

Neurotransmitters' white matter mapping unveils the neurochemical fingerprints of stroke

Received: 17 February 2024

Accepted: 25 February 2025

Published online: 15 March 2025



Pedro Nascimento Alves^{1,2}✉, Victor Nozais^{3,4}, Justine Y. Hansen⁵,
Maurizio Corbetta^{6,7,8}, Parashkev Nachev⁹, Isabel Pavão Martins^{1,2} &
Michel Thiebaut de Schotten^{3,4}

Distinctive patterns of brain neurotransmission frame determinant circuits for behavior. Understanding the relationship between their damage and the cognitive impairment provoked by brain lesions could provide insights into the pathophysiology and therapeutics of disabling disorders, like stroke. Yet, the challenges of neurotransmitter circuits mapping in vivo have hampered this investigation. Here, we developed an MRI white matter atlas of neurotransmitter circuits and created a method to chart how stroke damages neurotransmitter systems, which distinguishes pre and postsynaptic disruption. Our model, trained and tested in two large stroke patient samples, identified eight clusters with different neurochemical patterns. The associations with patients' cognitive profiles were scarce, denoting that a particular cognitive deficit might have finer underlying neurochemical disturbances that are unfit to the granularity of our analyses. These findings depict stroke neurochemical diaschisis patterns, provide insights into stroke cognitive deficits and potential treatments, and open a new window for tailored neurotransmitter modulation.

The discovery of neurotransmitters revolutionized our understanding of the nervous system. It commenced with a famous debate known as the “spark vs soup” regarding the peripheral nerves¹. Otto Loewi conducted a ground-breaking experiment in 1921, that laid the cornerstone for our understanding of neurochemical transmission. He demonstrated that extracts of frogs' hearts subjected to vagal stimulation slowed the rate of denervated hearts^{2,3}. Subsequent work on acetylcholine's role further solidified the concept of chemical communication at the neuromuscular junction⁴, an insight that would eventually unravel the complexities of synaptic transmission within the brain itself^{5–7}. It is within these intricate neurochemical pathways

that we framed crucial determinants of brain function and pathology^{8–13}.

Stroke, as a predominant cause of brain pathology¹⁴, orchestrates a cascade of cognitive and behavioral sequelae^{15,16}. The relationship between the neurotransmitter systems and deficits arising from stroke presents a promising avenue for exploration. Leveraging on Positron Emission Tomography (PET), ground-breaking work has linked serotonin receptor asymmetries to poststroke depression severity¹⁷, and recent Diffusion-Weighted Imaging (DWI) research connected cholinergic circuit integrity (i.e., the fornix) with long-term episodic and working memory improvements in stroke¹⁸. Yet, a comprehensive

¹Laboratório de Estudos de Linguagem, Centro de Estudos Egas Moniz, Faculdade de Medicina, Universidade de Lisboa, Lisbon, Portugal. ²Unidade de Acidentes Vasculares Cerebrais, Serviço de Neurologia, Departamento de Neurociências e Saúde Mental, Hospital de Santa Maria, ULSSM, Lisbon, Portugal.

³Groupe d'Imagerie Neurofonctionnelle, Institut des Maladies Neurodégénératives-UMR 5293, CNRS, CEA, University of Bordeaux, Bordeaux, France. ⁴Brain Connectivity and Behaviour Laboratory, Sorbonne Universities, Paris, France. ⁵Montréal Neurological Institute, McGill University, Montréal, QC, Canada.

⁶Clinica Neurologica, Department of Neuroscience, University of Padova, Padova, Italy. ⁷Padova Neuroscience Center, University of Padova, Padova, Italy.

⁸Venetian Institute of Molecular Medicine, Fondazione Biomedica, Padova, Italy. ⁹Queen Square Institute of Neurology, University College London, London, UK. ✉e-mail: pedronascimentoalves@gmail.com

in vivo mapping of these neurotransmitter circuits remains elusive, hampering the progress of targeted therapeutics.

The limited success of neurotransmitter-modulating drugs in clinical trials on stroke recovery underscores the need for more refined approaches¹⁹. For instance, whilst selective serotonin reuptake inhibitors show efficacy in treating poststroke depression, their impact on cognitive and functional recovery is inconsistent and marked by a high degree of response variability^{20–22}. Similarly, manipulating other neurotransmitter systems such as noradrenaline^{23–25}, acetylcholine^{26,27}, and dopamine²⁸ has seen limited therapeutic success, suggesting that a more nuanced approach, tailored to individual neurotransmitter profiles, might enhance therapeutic outcomes.

The recent publication of a neurotransmitter atlas by Hansen et al. offers a promising avenue for such personalized interventions²⁹. By compiling normative maps of receptor and transporter densities, this atlas is a pivotal reference for discerning the neurochemical profile of various brain disorders^{29–31}. Yet, its implementation in focal brain diseases involving white matter, like stroke, remains challenging.

The interaction between receptor and neurotransmitter depends on the preservation of the neurons and their receptors that receive the neurotransmitter (i.e., postsynaptic) as well as the integrity of the neuron responsible for producing the neurotransmitter (i.e., presynaptic). Hence, damage to the pre or postsynaptic neuron's axons disrupts the neurotransmitter circuits through neurochemical diaschisis, even if the synaptic structures, such as receptors and transporters, remain intact.

Here, we aimed to develop a method to chart stroke lesions onto neurotransmitter circuits, accounting for neurochemical diaschisis. To achieve this, we utilized the Functionnectome³², a recent method that projects values in the gray matter onto the white matter voxels based on their weighted connection probability. This method created a neurotransmitter white matter atlas representing the axonal projections of acetylcholine, dopamine, noradrenaline, and serotonin receptors and transporters. We then estimated the impact that individual stroke lesions would have on the neurotransmitter circuits indirectly, by differentiating presynaptic and postsynaptic disruption. Atlases and codes are freely available. We demonstrated that these measures can differentiate stroke lesions in discrete clusters with specific neurochemical profiles. Finally, we analyzed the behavioral and anatomical patterns of the identified neurochemical clusters, ultimately evidencing that a certain cognitive profile might have different underlying neurochemical bases.

Results

White matter neurotransmitter projection atlas

Normative location density maps of the acetylcholine, dopamine, noradrenaline and serotonin receptors and transporters were obtained from Hansen et al.²⁹. These maps were derived from 1200 healthy individuals' Positron Emission Tomographies. The following maps were extracted: acetylcholine receptors alpha4beta2 (42R) and muscarinic 1 (M1R); acetylcholine vesicular transporter (VACHT); dopamine receptors 1 (D1R) and 2 (D2R); dopamine transporter (DAT); noradrenaline transporter (NAT); serotonin receptors 1a (5HT1aR), 1b (5HT1bR), 2a (5HT2aR), 4 (5HT4R), and 6 (5HT6R); and serotonin transporter (SHTT).

To map receptors and transporters onto the white matter, we used the Functionnectome³². This tool projects gray matter voxel values onto the white matter according to the voxel-wise weighted probability of structural connection. Whole brain 7 T deterministic tractographies from 100 Human Connectome Project participants were used as anatomical priors. Histochemistry and neuronal tracing provided highly reliable anatomical knowledge about neurotransmitter circuits^{33–36}. Acetylcholine, dopamine, noradrenaline, and serotonin are produced in specific nuclei located in the brainstem and basal forebrain (Table 1)^{37–41}. The streamlines traversing the

neurotransmitter-producing nuclei were used to create the Functionnectome anatomical priors.

The obtained representative map of the neurotransmitter systems white matter projections is presented in Fig. 1. The lobar distribution was diversified, with a dominance of serotonin tracts in anterior and medial regions, acetylcholine in posterior regions, and noradrenaline and dopamine in orbitofrontal regions. Papez circuit's structures showed an acetylcholine predominance, namely the fornix, anterior and mediodorsal thalamic, and some temporal medial regions. The anterior thalamic radiations and the frontostriatal tracts were mainly noradrenergic and dopaminergic. In the brainstem, the posterior fibers were dominated by noradrenergic circuits, whereas the most anterior by serotonergic. The cerebellum was predominantly acetylcholinergic. Most of the white matter projection maps were asymmetric. The 5HT2aR, 5HT4R, 5HT6, SHTT, D1R, 42R, M1R and VACHT maps were mainly right-lateralized, while the 5HT1bR map was left-lateralized ($p < 0.05$, corrected for multiple comparisons). A statistically significant asymmetry was also found for 5HT1aR and D2R, but the effect sizes were small. The DAT white matter projection map did not present a significant lateralization. Asymmetries were also found in the location density maps. The 5HT1aR, D1R, D2R, DAT, 42R and M1R maps were predominantly right-lateralized, while the 5HT1bR, 5HT2aR, 5HT4R and 5HT6R maps were predominantly left-lateralized. A statistically significant asymmetry was also found for SHTT and VACHT, but the effect sizes were small. The voxel-wise interhemispheric difference maps are presented in the supplementary Table 1.

The projection maps for each receptor and transporter are available at <https://identifiers.org/neurovault.collection:15237>. The representative map of the neurotransmitter receptor and transporter location densities is presented in Fig. 2.

A supplementary data-driven analysis, without prior streamline selection, was also performed to explore neurotransmitters whose production is not associated with specific brainstem or basal forebrain nuclei. The following additional maps were analyzed²⁹: γ -aminobutyric acid (GABA) A receptor (GABA_AR), metabotropic glutamate receptor 5 (mGluR5), μ -opioid receptor (MOR), histamine 3 receptor (H3R) and cannabinoid receptor 1 (CB1R). The projection maps are available at <https://identifiers.org/neurovault.collection:17228>.

Pre and postsynaptic ratios

A neurotransmitter circuit may be disrupted presynaptically or postsynaptically. In presynaptic injury, the neurotransmitter release in the synaptic cleft decreases, and its interaction with receptors is reduced. Transporters are located in the presynaptic membrane (Fig. 3a). The lesion proportion of transporter location density maps and white matter projection maps were used as neuroimaging surrogates of presynaptic membrane and presynaptic axonal injury, respectively (Fig. 3b, left).

In postsynaptic injury, neurotransmitters are released in the synaptic cleft. However, the postsynaptic neuron does not mediate their effect, and there is a relative predominance of transporters over the receptors available. Receptors are located in the postsynaptic membrane. The lesion proportion of receptor location density maps and receptor white matter projection maps were used as neuroimaging surrogates of the postsynaptic membrane and postsynaptic axonal injury, respectively (Fig. 3b, right).

Quantifying the pre/post-synaptic unbalance can provide new premises of pharmacological modulation, namely with the tailored use of receptor agonists or transporter inhibitors. Therefore, we calculated a neuroimaging measure of the relative presynaptic injury of each receptor – the presynaptic ratio – and of the relative postsynaptic injury of each transporter – the postsynaptic ratio.

Then, we calculated the pre and postsynaptic ratios of two sets of stroke lesions and analyzed whether the individual neurotransmitter profiles would be grouped in different clusters. The first set (training

Table 1 | Fiber tracts selection criteria for the Functionnectome anatomical priors' generation

Neurotransmitter	ROI for streamline selection	Circuit	Atlas	Number of tractograms
Acetylcholine ⁸	Nucleus basalis of Meynert	Basal forebrain circuit	Zaborszky et al. stereotaxic probabilistic atlas ³⁷	186 980
–	Septal nuclei	–	–	–
–	Pedunculo-tegmental nuclei	Ponto-mesencephalic circuit	Brainstem navigator atlas ¹³⁵	–
–	Laterodorsal tegmental nuclei	–	–	–
Dopamine ¹³⁶	Substantia nigra, pars compacta	Nigrostriatal circuit	Brainstem navigator atlas ¹³⁷	166 734
–	Ventral tegmental area	Mesocortico-limbic circuit	Harvard Ascending Arousal Network Atlas ¹³⁸	–
Noradrenaline ¹³⁹	Locus coeruleus	Dorsal circuit	Brainstem navigator atlas ¹⁴⁰	129 176
–	Inferior and superior medullary reticular formation lateral nuclei	Ventral circuit	–	–
Serotonin ¹¹	Caudal-rostral linear raphe	Raphe system	Brainstem navigator atlas ^{140,141}	149 468
–	Dorsal raphe	–	–	–
–	Median raphe	–	–	–
–	Paramedian raphe	–	–	–
–	Raphe magnus	–	–	–
–	Raphe obscurus	–	–	–
–	Raphe pallidus	–	–	–

set) comprised 1333 acute ischemic stroke lesions from the University College London Hospitals acute stroke service, and the second (validation set) of 119 acute ischemic and 24 acute hemorrhagic stroke lesions from the Washington University School of Medicine in St. Louis. Both datasets are representative of the distribution of stroke lesions^{42,43}. The unsupervised k-means clustering algorithm was computed.

Figure 4 presents the neurotransmitter profiles of two example cases. Both caused a predominant imbalance of the serotonergic circuits: the first postsynaptically (serotonin postsynaptic ratio > 1; Fig. 4, left); the second presynaptically (serotonin presynaptic ratios > 1; Fig. 4, right).

The distribution of pre and postsynaptic ratios in the training and validation stroke sets is plotted in Supplementary Fig. 1. The distribution of pre and postsynaptic damage percentages is plotted in Supplementary Fig. 2.

The pre and postsynaptic ratios had a high cluster tendency: Hopkins statistics of 0.08 and 0.13 in the training and validation sets, respectively. The elbow method analysis showed that the optimal number of clusters was 8 in both sets.

Figure 5 shows the pre and postsynaptic ratios' distribution by cluster in the training and validation sets. Table 2 shows the effect sizes of the statistically significant associations in the validation set.

Behavioral and motor profiles of neurochemical clusters

Then, we analyzed if behavioral and motor profiles differed between neurochemical clusters. Behavioral and motor measures were available in the validation set. It included detailed behavioral and motor assessments in the acute phase (13 ± 4.9 days after stroke) and 3 months after stroke. The behavioral assessment covered the language, visuospatial attention, verbal and visuospatial memory, and depression domains.

The distributions of the behavioral and motor composite scores by the cluster at the 3 months post-stroke are presented in Fig. 6a. The average scores by test are presented in Supplementary Fig. 3. The acute phase assessments are presented in Supplementary Fig. 4a and b.

There was a statistically significant difference between clusters in the visuospatial attention (*p*-value = 0.017) and motor functions (*p*-

value = 0.023) domains. In pairwise comparisons, cluster 5 patients presented better visuospatial attention performance than the patients of clusters 1, 4, 6, and 8, and better motor functions than the patients of cluster 6.

To further evaluate the association between the behavioral and motor deficits and the neurochemical profiles, we performed a Uniform Manifold Approximation and Projection (UMAP) analysis. UMAP is a nonlinear dimensionality reduction technique that constructs a low-dimensional representation of high-dimensional data and preserves more of its global and local structure⁴⁴. In stroke, it has demonstrated better performance in disconnection-deficits predictions⁴⁵. The two-dimensional UMAP representation of the scaled behavioral and motor scores 3 months post-stroke and in the acute phase are presented in Fig. 6b and Supplementary Fig. 4c.

Then, we applied the density-based clustering algorithm HDBSCAN to the UMAP representation (<https://umap-learn.readthedocs.io>)⁴⁶ and evaluated the similarity between the neurochemical and the UMAP-derived behavioral and motor clusters. No matching was observed: Adjusted Rand Score of 0.016 and 0.005 for the 3 months and acute phase assessments, respectively (1 meaning perfect matching, 0 random labeling, and – 0.5 discordant clustering). We repeated the analysis with the patients with no missing behavioral and motor data (*n* = 69) at 3 months post-stroke and *n* = 70 at the acute phase). No matching was observed: Adjusted Rand Score of 0.028 and 0.022 for the 3 months and acute phase assessments, respectively (supplementary fig. 5).

Anatomical patterns of neurochemical clusters

We analyzed whether the neurochemical clusters were associated with different lesion anatomical patterns. Stroke lesion locations are not random. They follow the anatomical distribution of brain vasculature. With this analysis, we could understand if the neurochemical clusters observed could reflect stroke lesions' spatial clustering⁴⁷.

Stroke-associated brain dysfunction is caused not only by the direct impact of the lesion but also by disconnection and diaschisis⁴⁸. Therefore, we computed the structural disconnectome map associated with each lesion using the Disconnectome maps tool from the BCBtoolkit⁴⁹. The lesion topography and the structural disconnectome maps were compared between neurochemical clusters.

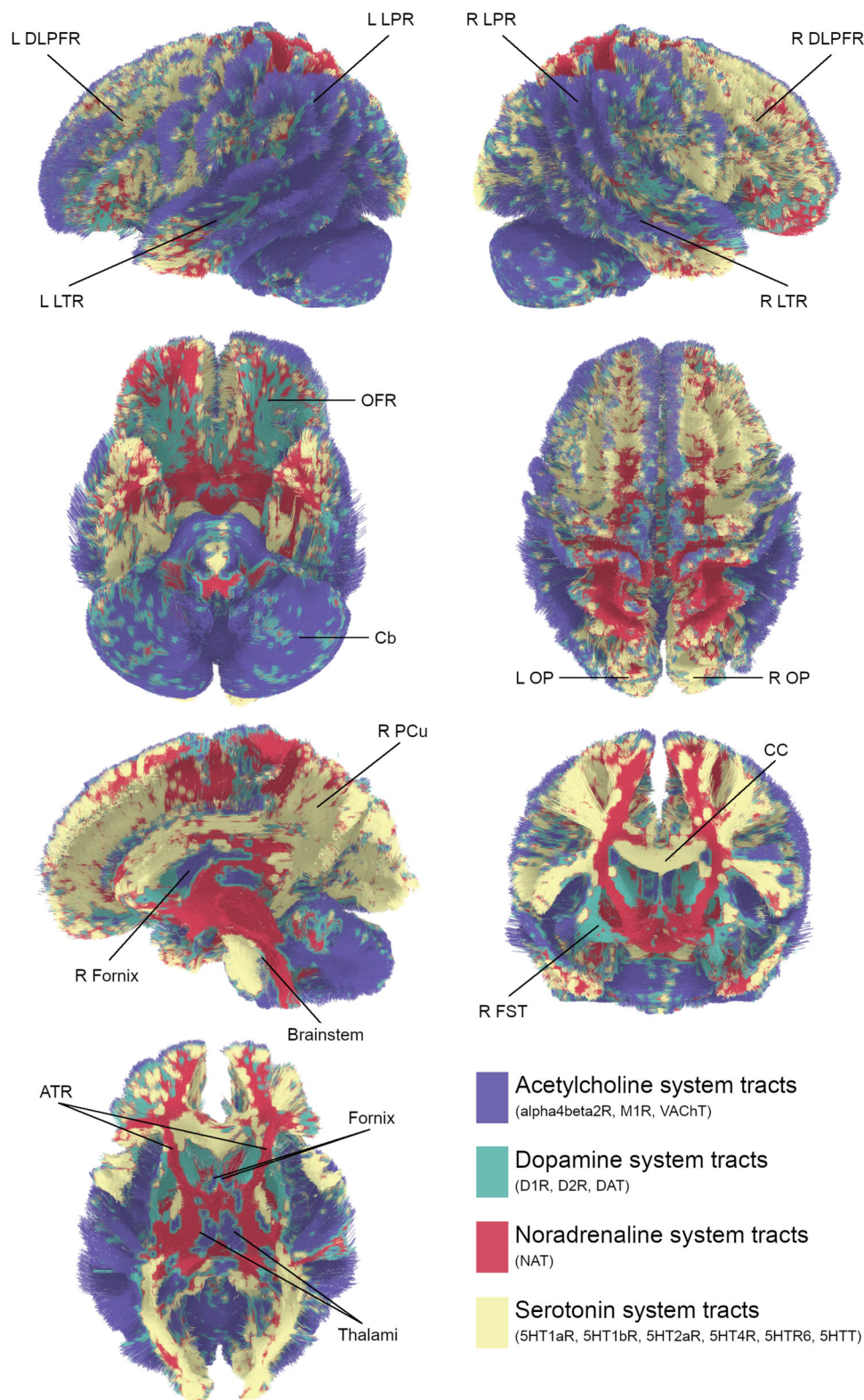


Fig. 1 | Representative map of the neurotransmitter systems white matter projections. The map was colored according to the neurotransmitter system of the map with the highest value at a voxel level. ATR anterior thalamic radiations, Cb cerebellum, CC corpus callosum, DLPFR dorsolateral prefrontal region, FST frontostriatal tracts, L left, LPR lateral parietal region, LTR lateral temporal region, OFR orbitofrontal region, OP occipital pole, PCu precuneus, R right, 5HT1aR serotonin receptor 1a, 5HT1bR serotonin receptor 1b, 5HT2aR serotonin receptor 2a, 5HT4R

serotonin receptor 4, 5HT6R serotonin receptor 6, 5HTT serotonin transporter, alpha4beta2R acetylcholine receptor alpha4beta2, D1R dopamine receptor 1, D2R dopamine receptor 2, DAT dopamine transporter, M1R muscarinic 1 receptor, NAT noradrenaline transporter, VAcHT acetylcholine vesicular transporter. The projection maps for each receptor and transporter are available at <https://identifiers.org/neurovault.collection:15237>.

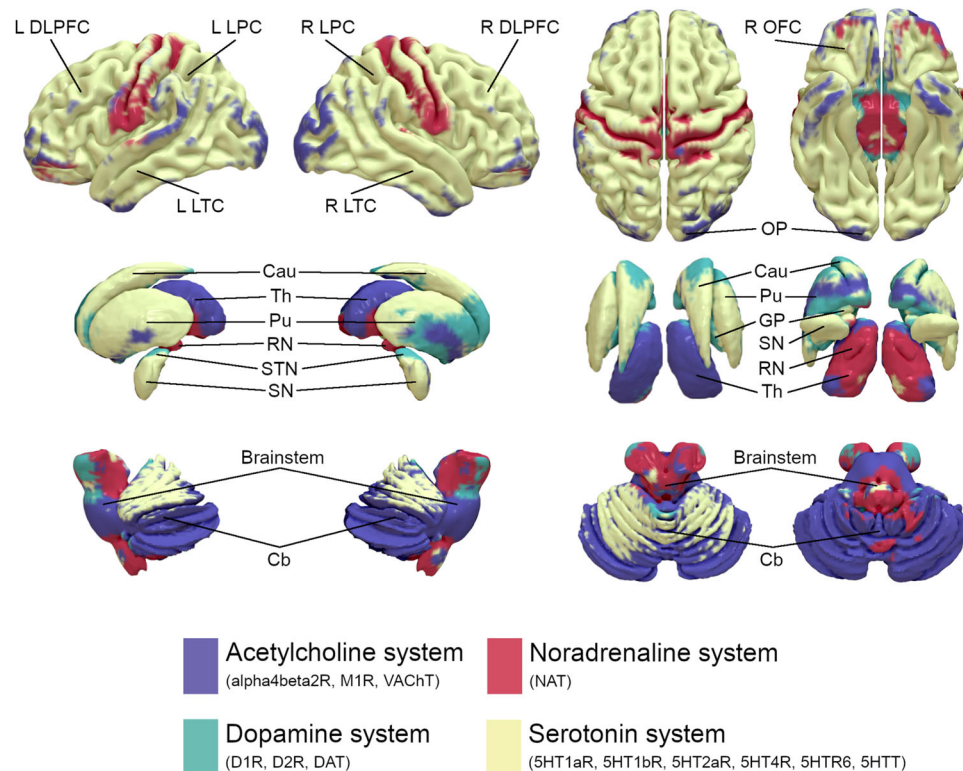


Fig. 2 | Representative map of the neurotransmitter systems location densities. The cortical (top row), basal ganglia (middle row), and brainstem and cerebellar (bottom row) surfaces are represented on the left (first column), right (second column), superior (third column), and inferior (fourth column) views. The map was colored according to the neurotransmitter system of the map (either receptor or transporter) with the highest value at a voxel level. Cau caudate nucleus, Cb cerebellum, DLPFC dorsolateral prefrontal cortex, L left, LPC lateral parietal cortex, LTC lateral temporal cortex, OFC orbitofrontal cortex, OP occipital pole, Pu pulvinar, R

right, RN red nucleus, SN substantia nigra, STN subthalamic nucleus, Th thalamus. 5HT1aR serotonin receptor 1a, 5HT1bR serotonin receptor 1b, 5HT2aR serotonin receptor 2a, 5HT4R serotonin receptor 4, 5HT6R serotonin receptor 6, 5HTT serotonin transporter, alpha4beta2R acetylcholine receptor alpha4beta2, D1R dopamine receptor 1, D2R dopamine receptor 2, DAT dopamine transporter, M1R muscarinic 1 receptor, NAT noradrenaline transporter, VACHT acetylcholine vesicular transporter.

Figure 7 presents the statistically significant associations of the neurochemical clusters with the lesion and structural disconnectome maps, in the validation set.

The cluster 1 patients presented a significantly higher probability of lesion in the left occipito-temporo-parietal regions, and a higher probability of structural disconnection in the splenium of the corpus callosum and left occipito-parietal regions. They had a lower probability of lesion of the right lenticular nucleus and a lower probability of structural disconnection of the brainstem, thalami, lenticular nuclei, frontal-medial regions bilaterally, and body of corpus callosum.

The cluster 2 patients had a significantly higher probability of lesion in the left pons and right medial thalamus, and a higher probability of structural disconnection of the pons, posterior brainstem and thalami. They had a lower probability of disconnection in small, antero-superior regions of the corona radiata.

The cluster 4 patients presented a significantly higher probability of lesion of the right prefrontal cortex, particularly of its ventrolateral region, and a higher probability of structural disconnection of the right prefrontal cortex, body, and genu of the corpus callosum, and dorsal frontoparietal regions bilaterally.

The cluster 5 patients had a significantly higher probability of lesion of the right cerebellar hemisphere and a higher probability of structural disconnection of the cerebellum, pons, and medial midbrain bilaterally. They had a significantly lower probability of lesion of the left corona radiata and a lower probability of structural disconnection in the lateral midbrain, in a wide extension of fronto-parieto-occipital white matter, and the body and splenium of the corpus callosum.

No statistically significant differences existed in clusters 3, 6, 7, and 8.

Validation of synaptic ratio analysis

To validate the pre and postsynaptic ratio analysis, we systematically searched for stroke cases that reported the clinical response to neurotransmitter-modulating drugs and with images of lesion topography available. According to our model, patients with predominant presynaptic damage would clinically improve with receptor agonists or inhibitors of degradation enzymes located postsynaptically and have no response to reuptake inhibitors. Patients with predominant postsynaptic disruption would have the reverse pattern of response. We included patients with poststroke cognitive deficits treated with acetylcholinesterase inhibitors, poststroke parkinsonism medicated with dopamine receptor agonists, poststroke pathological laughing and crying treated with selective serotonin reuptake inhibitors, and poststroke apathy medicated with any class of acetylcholinergic, dopaminergic or serotonergic drug. These poststroke syndromes are known to have a heterogenous response to neurotransmitter-modulating drugs^{50–53}.

We found 22 reports (Table 3). Our method correctly predicted the observed pharmacological response in 17 cases (accuracy: 77%; sensitivity: 75%; specificity: 83%). In 12 cases, we predicted clinical improvement, and it was observed; in 5 cases, we predicted no clinical improvement, and it was not observed; in 4 cases, we predicted no clinical improvement, but an improvement was observed; in 1 case, we predicted clinical improvement, but it was not observed. The association between prediction and observed clinical response was

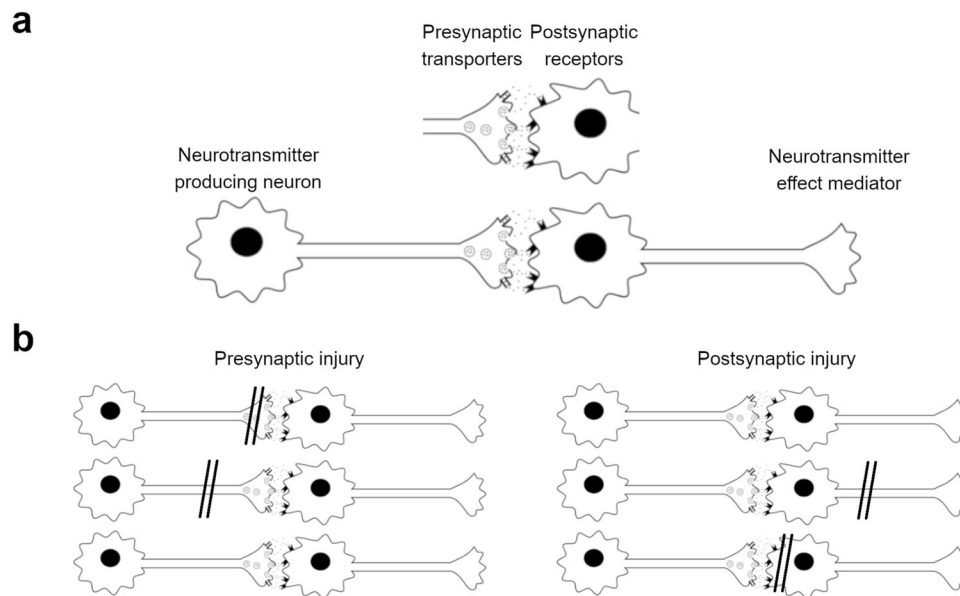


Fig. 3 | Neuronal model and synaptic ratios. a Schematic representation of the synapse basic structure. **b** Illustration of predominantly presynaptic and postsynaptic injuries.

statistically significant (Fisher's exact test; p -value = 0.023). The individual stroke lesion maps and pre and postsynaptic ratio graphs are presented in the supplementary Table 3.

We also ranked the drugs used by their likelihood of causing an improvement according to individual pre and postsynaptic ratio graphs. Drugs were categorized into six classes, corresponding to their predominantly pre or postsynaptic action in acetylcholinergic, dopaminergic, and serotonergic circuits. Accordingly, ranks varied from 1 to 6: 1 corresponded to the highest synaptic ratio, i.e., the highest probability of improvement; 6 corresponded to the lowest synaptic ratio, i.e., the lowest probability of improvement. This analysis showed that patients who clinically improved were treated with drugs with significantly better improvement likelihood ranks than patients who had no response (Mann-Whitney test; p -value = 0.020; improvement group, $n = 16$, median [interquartile range] = 3 [2–3.5]; no response group, $n = 6$, median [interquartile range] = 5.5 [4–6]). The individual drug ranks are reported in the supplementary Table 3.

Discussion

We present a novel approach for creating a white matter atlas of the neurotransmitter systems and a method for analyzing the impact of focal lesions on neurotransmitter circuits. We demonstrated the existence of distinct clusters of stroke lesions with unique presynaptic and postsynaptic neurotransmitter injury profiles alongside associated behavioral and anatomical characteristics. Our results underscore the intricate relationship between neurotransmitter disruption and post-stroke outcome.

Our atlas aligns well with existing histochemical knowledge of neurotransmitter circuits. For instance, identifying the fornix and thalamic fibers as predominantly acetylcholinergic aligns with previous findings in animal studies. In rats, acetyltransferase immunoreactivity is found in the fornix, and these neurons have projections to the hippocampus and the retrosplenial cortex^{54,55}. Deep brain stimulation of the fornix increases the acetylcholine levels in the rat hippocampus⁵⁶ and induces memory flashbacks in humans with Alzheimer's disease⁵⁷. The thalamus is also an essential cholinergic relay across species^{58–61}. This congruence extends to the dopaminergic and noradrenergic systems, particularly in the frontostriatal fibers and the orbitofrontal region, corroborating reports from rodents and animal studies. The fibers in the frontostriatal pathway, specifically those in

the orbitofrontal region, are primarily associated with dopamine circuits. Through retrograde labeling, it was discovered that neurons expressing D1 and D2 receptors in the prefrontal cortex of mice have separate projections to the striatum and midbrain⁶². These neurons integrate the dopaminergic mesocorticolimbic circuits, essential to human behavioral and mental functioning^{63,64}. Other fibers in the orbitofrontal region belonged predominantly to noradrenaline circuits. Some of them are part of the anterior thalamic radiations. The thalamus is rich in adrenoceptors⁶⁵. In addition, the locus coeruleus establishes connections with the orbitofrontal cortex directly or through thalamo-striatal connections^{65,66}. Together prefrontal cortex's dopaminergic and noradrenergic systems are known to interact, regulating cognition and behavior, and leading to symptoms when disrupted^{66–68}. The correspondence between our results and the well-established histochemical and clinical knowledge indirectly supports the validity of our method. In line with this, the interhemispheric asymmetry we report in our study was concordant with previous evidence from the literature. In zebrafish, it was shown that the acetylcholine habenula-interpeduncular pathway is asymmetric⁶⁹. In rats, the distribution of the muscarinic acetylcholine receptor is right-lateralized at the cortical level, and the dopamine levels are asymmetric in the forebrain and midbrain^{70,71}. In humans, Kranz and colleagues demonstrated asymmetries of serotonin transporter distribution in the temporal and frontal cortices, anterior cingulate, hippocampus, caudate, and thalamus using PET⁷². Tomer and colleagues reported asymmetries of dopamine D2 receptors in the striatum and frontal and temporal cortices⁷³.

Importantly, the innovation of our tool lies in its ability to dissociate the pre and postsynaptic impacts of lesions on neurotransmitter circuits. This approach has significant implications for clinical intervention since receptor agonists or transporter inhibitors' efficacy might depend on the nature of the synaptic dysfunction. For example, a receptor agonist is likely ineffective if the lesion causes a predominant postsynaptic dysfunction. Conversely, in a predominantly presynaptic dysfunction, using transporter inhibitors would not be plausible, but receptor agonists could partially restore the circuit's activity. Receptor stimulation is an important determinant of neurons' activity and brain functions. In experimental cultures, rodents' mid-brain dopamine-producing neurons tend to die spontaneously by apoptosis⁷⁴. These neurons are characterized by excitatory

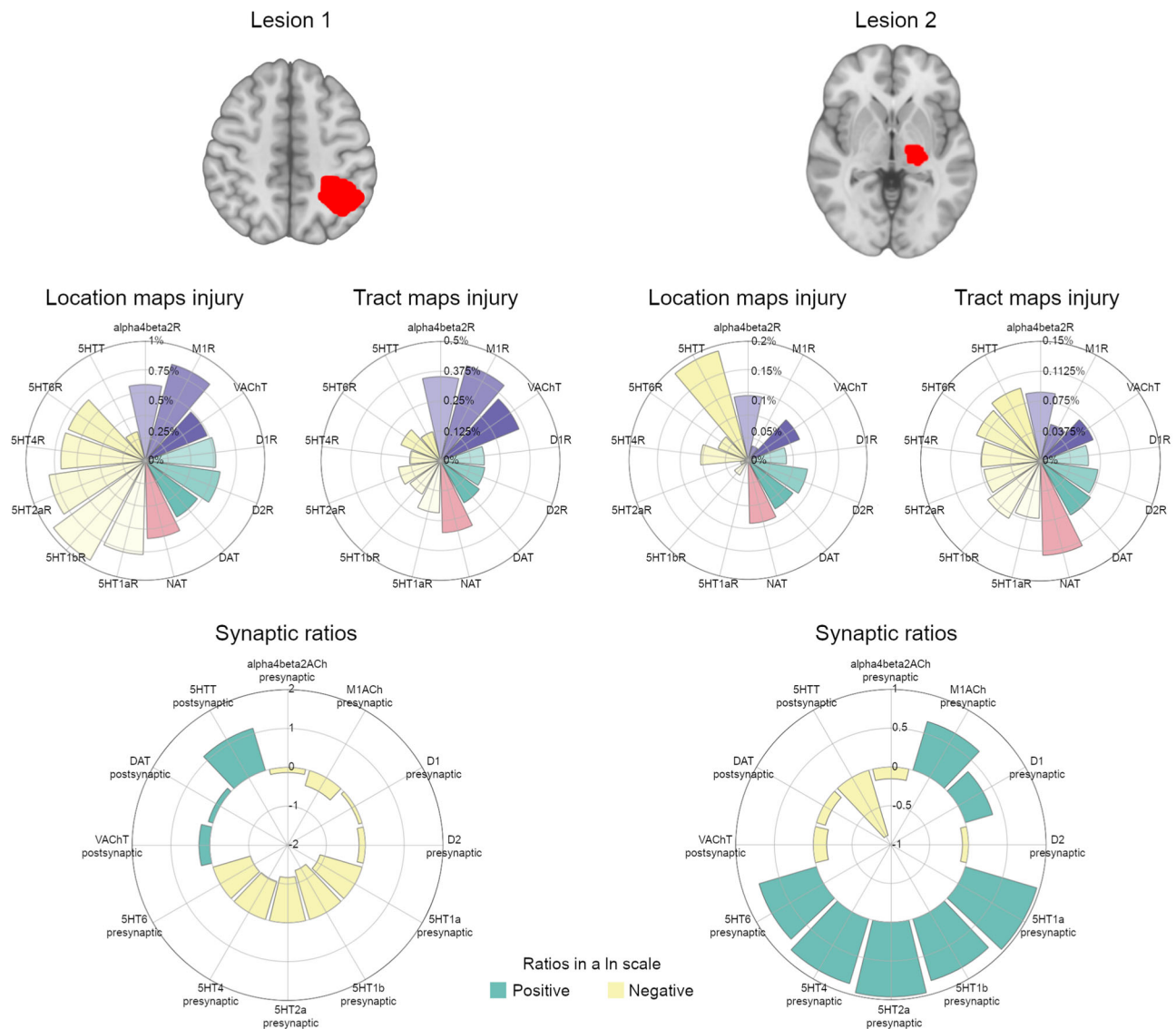


Fig. 4 | Two example cases of pre and postsynaptic ratio calculation. Top row – Lesion mask of two left hemisphere stroke lesions. Middle row – Percentage of each neurotransmitter system disrupted by the lesion, according to the receptor and transporter location density (location maps injury) and white matter projections (tract maps injury). Bottom row – Synaptic ratios presented in a natural logarithmic scale. 5HT1aR serotonin receptor 1a, 5HT1bR serotonin receptor 1b, 5HT2aR

serotonin receptor 2a, 5HT4R serotonin receptor 4, 5HT6R serotonin receptor 6 5HTT serotonin transporter, alpha4beta2R acetylcholine receptor alpha4beta2, D1R dopamine receptor 1, D2R dopamine receptor 2, DAT dopamine transporter, M1R muscarinic 1 receptor, NAT noradrenaline transporter, VAcHT acetylcholine vesicular transporter. Source data are provided as a Source Data file.

acetylcholine nicotinic receptors, and their cell death process can be slowed down by acetylcholine nicotinic agonists⁷⁵. In the brain, the pedunculopontine nuclei provide acetylcholinergic stimulation of midbrain dopaminergic nuclei⁷⁶. In monkey models of Parkinsonism and humans with Parkinson's disease, a correlation exists between the loss of pedunculopontine cholinergic neurons and the severity of gait impairment⁷⁷. Another example is the close interaction between serotonin and noradrenaline systems⁷⁸. Serotonin agonists increase the noradrenaline release in the hippocampus of rats⁷⁹. When mice experience left medial prefrontal stroke, they suffer from learning deficits and reduced depression-like behaviors. These mice also have reduced serotonin levels, associated with scarcer noradrenaline projections in different brain regions⁸⁰. Fluoxetine, a selective serotonin reuptake inhibitor, partially reverses the animals' behavior phenotype. Interestingly, at the histochemical level, it also partially restores the serotonin and noradrenaline projections⁸⁰. Our methods, together with this insight, could guide more targeted and effective treatments

for stroke and other focal brain lesions by fostering the development of neurochemically tailored clinical trials.

The sparse associations between the neurotransmitter profiles and the behavioral outcomes highlight the complexity of brain function and the multifaceted roles of neurotransmitters, i.e., various neurotransmitters support the brain circuits underlying a certain cognitive function⁸¹. For instance, in language disorders, the gray matter volume alterations of patients with primary progressive aphasia are spatially correlated with the serotonin, dopamine, and glutamatergic pathways⁸². Regarding memory, despite the core role of acetylcholine⁸³, other neurotransmitters have a demonstrated involvement, such as serotonin⁸⁴, dopamine, and noradrenaline^{85,86}. Concerning visuospatial attention, we have recently shown that the ventral and dorsal attention networks are spatially correlated with the distribution of acetylcholine nicotinic receptors and dopamine and serotonin transporters¹³. In depression, serotonin, dopamine, and noradrenaline are associated with different depressive symptoms⁸⁷.



Fig. 5 | Clusters of stroke lesions pre and postsynaptic ratios. a Training set. The sample sizes for clusters 1 to 8 are, respectively, 255, 89, 96, 452, 87, 121, 67, and 166. **b** Validation set. The sample sizes for clusters 1 to 8 are, respectively, 32, 18, 5, 39, 10, 19, 2, and 18. Ratios are presented in a natural logarithmic scale. The box plots display the data distribution with the following elements: the central line represents the median (50th percentile); the box bounds indicate the interquartile range (25th and 75th percentiles); the whiskers extend to the minima and maxima within 1.5 times the interquartile range; and any points beyond the whiskers represent outliers. Asterisks indicate the statistically significant associations in the validation set:

one-sided one-sample t-test or Wilcoxon test, depending on the data distribution; Bonferroni correction for multiple comparisons: p -value < 0.0042. 5HT1aR serotonin receptor 1a, 5HT1bR serotonin receptor 1b, 5HT2aR serotonin receptor 2a, 5HT4R serotonin receptor 4, 5HT6R serotonin receptor 6, 5HTT serotonin transporter, alpha4beta2R acetylcholine receptor alpha4beta2, D1R dopamine receptor 1, D2R dopamine receptor 2, DAT dopamine transporter, MIR, muscarinic 1 receptor, NAT noradrenaline transporter, VAcHT acetylcholine vesicular transporter. Source data are provided as a Source Data file.

Remarkably, the sparse association between behavior and neurotransmitter profiles is particularly relevant in understanding why nonspecific pharmacological treatments in post-stroke cognitive deficits have shown limited efficacy^{19,26–28}.

We have identified three different patterns of lesion that lead to varying neurochemical profiles. Cluster 1 is characterized by acetylcholine and serotonin circuits postsynaptic deficits, while brainstem fibers, where neurotransmitter-producing presynaptic neurons are located, and medial frontostriatal and frontothalamic fibers, where dopamine and noradrenaline are predominant, are spared. On the other hand, cluster 2 is associated with disconnection of the brainstem fibers and a presynaptic injury of serotonin and acetylcholine circuits. Cluster 5, on the other hand, spares frontal-parietal-occipital regions and corpus callosum, and its performance in visuospatial attention and motor tasks is significantly better than most of the other clusters. The lesion topography statistical maps do not follow the spatial distribution of brain vasculature⁸⁸. They do not overlap single vascular

territories of lesion or lesion sparing. Ischemic strokes involving more than one vascular territory are a minority, occurring in 2 to 9% of cases^{89–91}. The frequency of multiple lesions in hemorrhagic strokes is even lower⁹². Therefore, the presented neurochemical clusters do not primarily emerge from the spatial clustering of stroke lesions⁴⁷.

Despite these advancements, our study also acknowledges certain limitations. The range of neurotransmitters examined, while neuropharmacologically relevant, is not exhaustive. Moreover, our approach focuses on macrostructural analyses and does not delve into the complexity of microcircuits and glial interactions. It is also important to note that our model is based on structural injury and may not fully account for unbalanced circuit hyperfunction. In addition, despite the usefulness of k-means clustering analysis for understanding underlying patterns in synaptic ratios, it is a descriptive method and may not fully capture the most biologically appropriate data grouping. Finally, the calculated presynaptic and postsynaptic disruption ratios are

Table 2 | Effect sizes of the statistically significant associations in the validation set

	Statistically significant ratios		Effect size*
Cluster 1	Acetylcholine postsynaptic	VACHT	1.16
	Serotonin postsynaptic	5HTT	0.87
Cluster 2	Acetylcholine presynaptic	M1R	5.06
	Serotonin presynaptic	5HT1aR	1.05
	–	5HT1bR	1.05
	–	5HT2aR	1.05
	–	5HT4R	3.36
	–	5HT6R	3.86
Cluster 3	Acetylcholine presynaptic	42R	3.82
	–	M1R	4.10
	Dopamine postsynaptic	DAT	2.95
	Serotonin presynaptic	5HT1aR	3.91
	–	5HT1bR	5.44
	–	5HT2aR	4.82
	–	5HT6R	3.32
	–	–	–
Cluster 4	–	–	–
	Acetylcholine presynaptic	M1R	0.98
	Dopamine presynaptic	D1R	0.98
	Serotonin presynaptic	5HT1aR	0.98
	–	5HT1bR	11.23
	–	5HT2aR	0.98
Cluster 5	–	5HT4R	6.28
	Acetylcholine presynaptic	42R	2.81
	–	M1R	3.28
	Dopamine postsynaptic	DAT	3.34
	Serotonin presynaptic	5HT1aR	2.76
	–	5HT1bR	2.26
Cluster 6	–	5HT2aR	3.70
	–	5HT6R	1.03
	–	–	–
	–	–	–
Cluster 7	–	–	–
	–	–	–
Cluster 8	Dopamine postsynaptic	DAT	1.08
	Serotonin presynaptic	5HT1aR	1.50
	–	5HT1bR	1.20
	–	5HT2aR	1.47
	–	5HT4R	1.05
	–	5HT6R	1.05

*Effect sizes represent Cohen's d statistic or its nonparametric equivalent, according to data distribution. 5HT1aR serotonin receptor 1a, 5HT1bR serotonin receptor 1b, 5HT2aR serotonin receptor 2a, 5HT4R serotonin receptor 4, 5HT6R serotonin receptor 6, 5HTT serotonin transporter, 42R acetylcholine receptor alpha4beta2, D1R dopamine receptor 1, D2R dopamine receptor 2, DAT dopamine transporter, M1R muscarinic 1 receptor, NAT noradrenaline transporter, VACHT acetylcholine vesicular transporter.

indirect estimations, not direct measures. While the validation performed in published case reports is promising, future additional direct validation in larger samples not constrained to publication biases is needed. Nuclear medicine imaging techniques, namely PET and Single Photon Emission Computed Tomography (SPECT), can directly map the neurotransmitter receptor or transporter density. However, the need for different radioligands to chart the impact of patients' lesions on neurotransmitter circuits would be unsafe and unfeasible. The white matter projections were not made on patients' tractograms but

on tractographies from the Human Connectome Project (HCP) data. Although it has been shown that normative structural data predict stroke patients' outcomes^{45,93} and is a valid surrogate of individual white matter⁴⁸, it does not capture subject-specific variations. The missing data can constitute a bias in the behavioral and motor analysis.

In conclusion, our study provides valuable insight into the neurochemical underpinning of stroke lesions and offers a novel tool for analyzing neurotransmitter circuit disruption. This work advances our understanding of stroke pathophysiology and opens new avenues for targeted neurochemical modulation, potentially improving post-stroke rehabilitation strategies and patient outcomes.

Methods

Neurotransmitter receptor and transporter location densities
Normative neurotransmitter receptor and transporter location density maps were obtained from the work of Hansen and colleagues (https://github.com/netneurolab/hansen_receptors)²⁹. These maps were derived from the collection of 1200 healthy individuals registered to the MNII52 space. We extracted the following maps: acetylcholine receptors 42R⁹⁴ and M1R⁹⁵; acetylcholine transporter VACHT^{96,97}; dopamine receptors D1R⁹⁸ and D2R^{99–102}; dopamine transporter DAT^{103,104}; noradrenaline transporter NAT¹⁰⁵; serotonin receptors 5HT1aR^{106,107}, 5HT1bR^{106–108}, 5HT2aR^{106,107,109}, 5HT4R¹⁰⁶ and 5HT6R¹¹⁰; serotonin transporter 5HTT^{106,107}; γ-aminobutyric acid receptor GABA_AR^{103,111}; glutamate receptor mGluR5^{112,113}; μ-opioid receptor^{114,115}; histamine H3 receptor¹¹⁶; and cannabinoid receptor 1^{117,118}. Because the PET binding/uptake values varied from tracer to tracer, we scaled the maps into zero to one interval, representing each tracer's minimum and maximum concentrations. When more than one tracer map was available for a specific receptor or transporter, the median value was calculated.

To create a single illustrative map of the four neurotransmitter systems, we calculated the maximum value at each voxel and labeled it accordingly (i.e., corresponding to the acetylcholine, dopamine, noradrenaline, or serotonin systems). The map was projected onto the cortical and basal ganglia surfaces using Surfice (<https://www.nitrc.org/projects/surfice/>; Fig. 2).

White matter mapping of receptors and transporters

To map receptors and transporters on the white matter, we used the Functionnectome (<https://github.com/NotaCS/Functionnectome>). This tool projects gray matter voxel values onto the white matter according to the voxel-wise weighted probability of structural connection with other voxels³². Normative structural probability maps derived from whole brain deterministic tractography of 7 T diffusion-weighted MRIs from 100 HCP participants¹¹⁹ are input as priors. Accordingly, we calculated the probability of each brain voxel being structurally connected with the other voxels of the brain^{32,49}. If two voxels had streamlines intersecting them on high-resolution tractography, they were considered connected. The classification was binary, i.e., connected or not connected. The binary structural connectivity maps obtained from the 100 HCP participants were averaged to obtain a representative map at the population level of the probability of connection between a reference voxel and white matter voxels. The normative maps' values varied from 0 to 1: 0 when the voxels were not connected in any of the 100 HCP tractographies and 1 when they were connected in all. To project gray matter voxel values onto a specific white matter voxel, the Functionnectome calculates the average of all gray matter voxel values weighted by the probabilities of the white matter voxel being connected with those gray matter voxels. The step is repeated for every white matter voxel³². The tractographies were processed according to the protocol described in Thiebaut de Schotten et al.¹²⁰ and are freely available at <https://osf.io/5zqwg/> and <http://www.bcbilab.com/>.

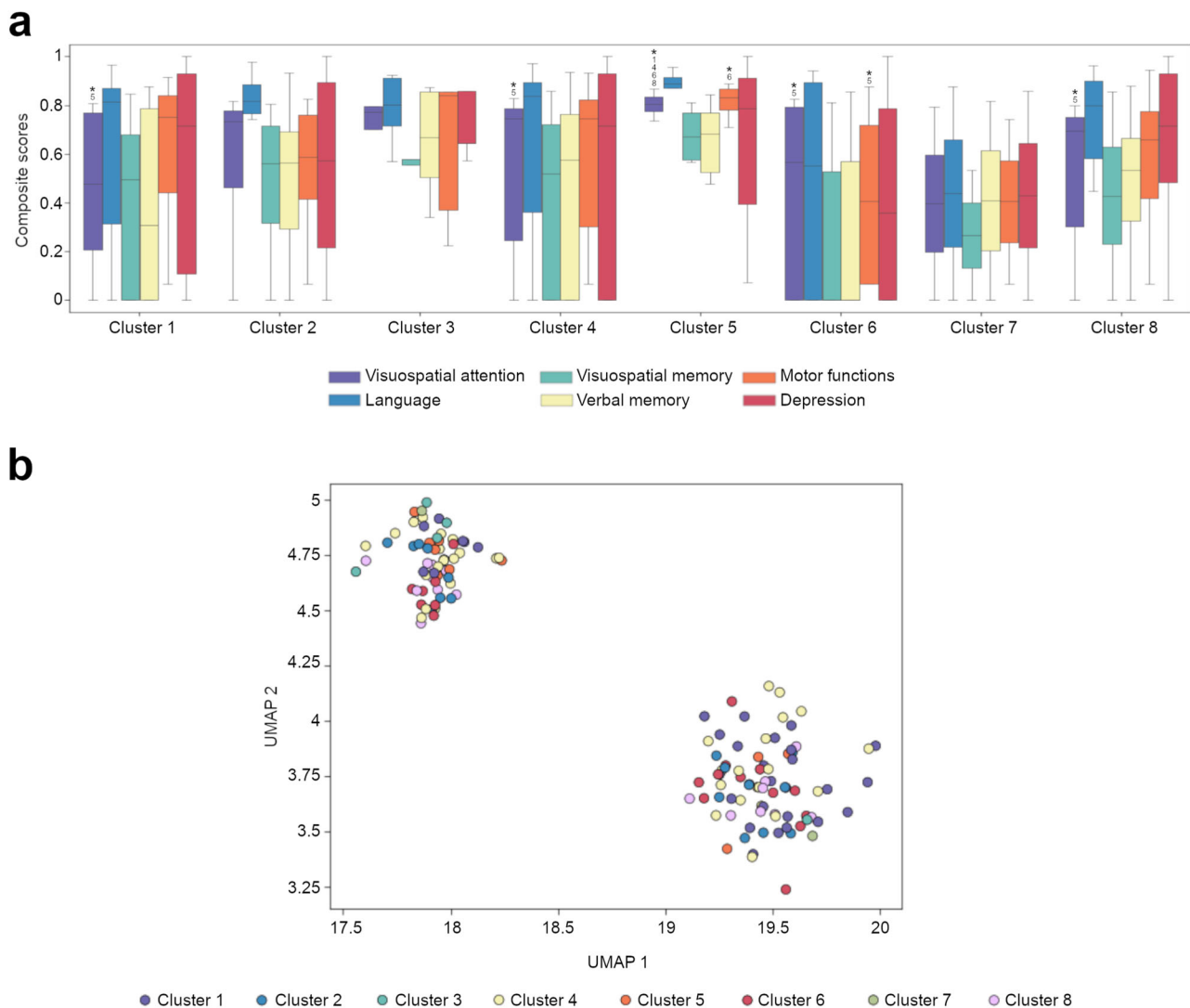


Fig. 6 | Behavioral and motor profiles by neurochemical cluster (3 months post-stroke assessment). **a** Distribution of composite scores by neurochemical cluster. The box plots display the data distribution with the following elements: the central line represents the median (50th percentile); the box bounds indicate the interquartile range (25th and 75th percentiles); the whiskers extend to the minima and maxima within 1.5 times the interquartile range; and any points beyond the whiskers represent outliers. The Kruskal-Wallis test was calculated to investigate if the composite scores differed between clusters. The two-sided Dunn's test was applied to perform pairwise comparisons when statistically significant differences

occurred. A Bonferroni correction for multiple comparisons was applied (p -value < 0.0018 for statistical significance). Asterisks indicate the statistically significant differences in pairwise comparisons. The associated numbers represent the cluster with which a significant difference was found. The sample sizes for clusters 1 to 8 are, respectively, 32, 18, 5, 39, 10, 19, 2, and 18. **b** Uniform Manifold Approximation and Projection (UMAP) analysis of the scaled behavioral and motor scores. The dot colors represent the neurochemical cluster to which the patients belong. Source data are provided as a Source Data file.

Based on histochemistry and neuronal tracing, the prior anatomical knowledge about neurotransmitter circuits is highly reliable. The main analysis focused on neurotransmitters produced in the specific brainstem and basal forebrain nuclei, namely acetylcholine, dopamine, noradrenaline, and serotonin. We selected the streamlines traversing the neurotransmitter-producing nuclei using the MRtrix3's tool "tckedit"¹²¹. We selected traversing streamlines instead of exclusively the streamlines terminating in nuclei because tractography does not detect synapses, and a true axonal termination might not correspond to a fiber tract termination in tractography^{122–124}. The resulting tractograms were used to create the Functionconnectome anatomical priors. Table 1 presents the selection criteria applied. A representative map of the four neurotransmitters white matter projections was calculated by determining the maximum value at each voxel, as performed in the previous section. To analyze brain asymmetries, the hemispheres

were flipped, and the interhemispheric differences were calculated at a voxel level. The one-sample t -test or the Wilcoxon test (according to data distribution) were computed to investigate whether the difference map values significantly differed from zero. A Bonferroni correction for multiple comparisons was applied (alpha level set at 0.0042 for statistical significance). The Cohen's d statistic or its nonparametric equivalent were calculated to estimate the effect size of the statistically significant associations. The same procedure was applied to assess asymmetry in the location density maps.

We also performed a supplementary data-driven analysis in which no anatomical constraints were made in the tractograms. This analysis explored neurotransmitters whose production is not associated with specific brainstem or basal forebrain nuclei. The following additional maps were examined²⁹: GABA_AR, mGluR5, μ -opioid receptor, histamine 3 receptor, and cannabinoid receptor 1.

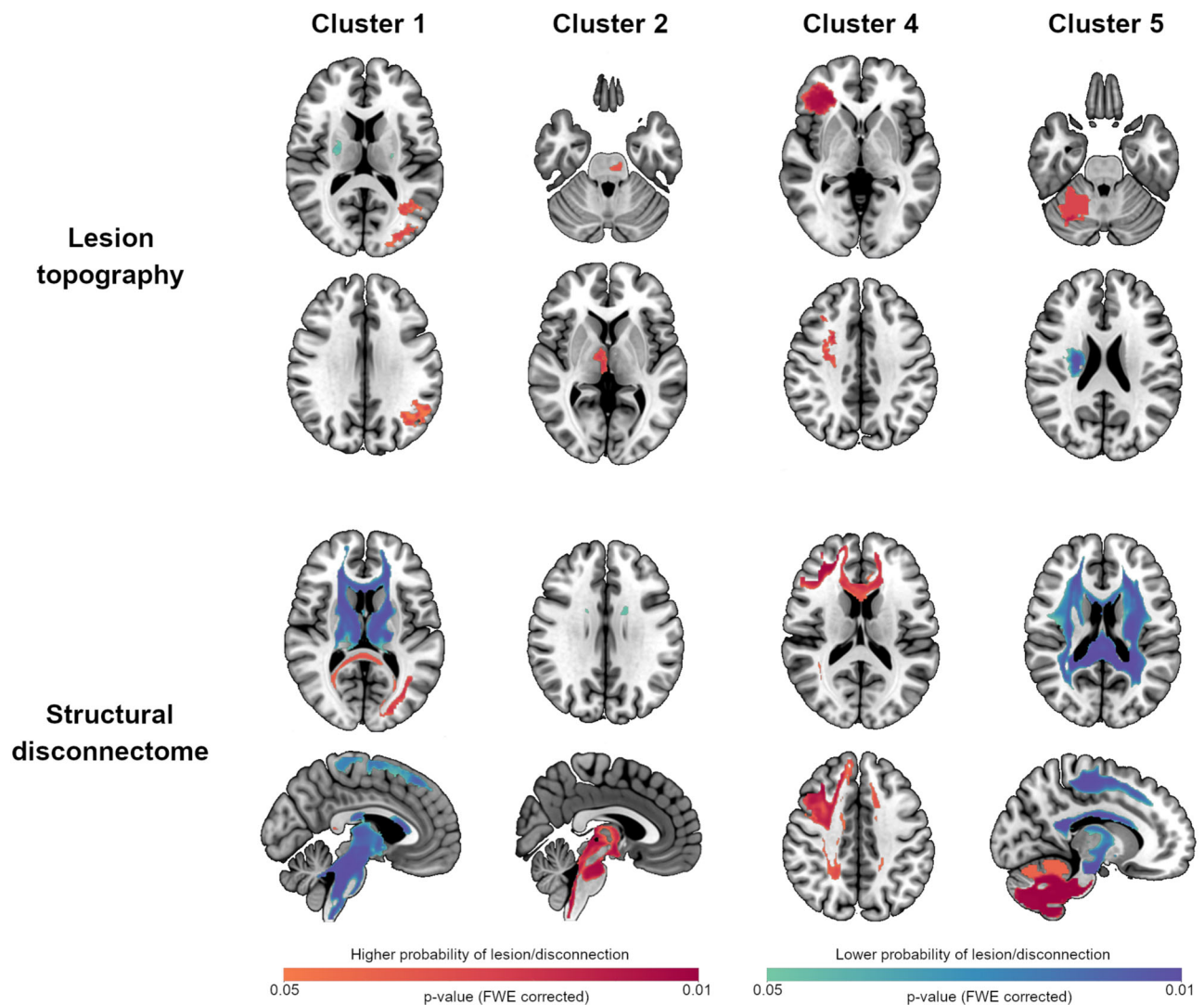


Fig. 7 | Anatomical patterns of neurochemical clusters. Statistical maps of the comparison between the lesion topography (upper rows) and structural disconnectome (lower rows) maps of each neurochemical cluster with the remaining clusters, in the validation set. The orange-red and the cyan-blue colourmaps represent the significantly higher or lower probability of lesion/disconnection, respectively (nonparametric two-sample unpaired permutation test, based on

5000 permutations). *P*-values were family-wise error rate (FWE) corrected for multiple comparisons. Only the clusters with statistically significant associations are shown. Images are presented according to the radiological convention (in axial slices, the left hemisphere corresponds to the right side of the picture). The sample sizes for clusters 1, 2, 4 and 5 are, respectively, 32, 18, 39, and 10.

Pre and postsynaptic ratios

The presynaptic ratio was calculated by dividing the proportion of the presynaptic by the proportion of the postsynaptic structural damages. Transporters are located in the presynaptic membrane (Fig. 3a). First, we calculated the proportion of transporter damage by dividing the sum of its location density map voxels overlapped by the stroke lesion by the sum of all its location density map voxels. Then, we calculated the proportion of transporter white matter projection damage by dividing the sum of its white matter projection map voxels overlapped by the stroke lesion by the sum of all its white matter projection map voxels. The proportion of the presynaptic damage was defined as the maximum value of these two proportions (i.e., of the proportion of transporter damage and the proportion of transporter white matter projection damage). Inversely, receptors are located in the postsynaptic membrane (Fig. 3a). Therefore, we defined the proportion of the postsynaptic damage as the maximum value of the proportion of receptor damage and the proportion of receptor white matter projection

damage. The formula for the presynaptic ratio was as follows:

$$\text{presynaptic ratio} = \frac{\max \left(\frac{\sum_i M^{\text{trans_loc}}_i}{\sum_i T^{\text{trans_loc}}_i}, \frac{\sum_i M^{\text{trans_tract}}_i}{\sum_i T^{\text{trans_tract}}_i} \right)}{\max \left(\frac{\sum_i M^{\text{recep_loc}}_i}{\sum_i T^{\text{recep_loc}}_i}, \frac{\sum_i M^{\text{recep_tract}}_i}{\sum_i T^{\text{recep_tract}}_i} \right)}$$

where: *i*, voxel value; max, maximum; *M*, lesion mask voxels; recep_loc, receptor location density map; recep_tract, receptor white matter projection map; *T*, all map voxels; trans_loc, transporter location density map; trans_tract, transporter white matter projection map.

The postsynaptic ratio was calculated by dividing the proportion of the postsynaptic by the proportion of the presynaptic structural damages (Fig. 3c, right). The postsynaptic ratio is not redundant with the presynaptic ratio because each transporter might be associated with more than one receptor. In this case, the proportion of postsynaptic structural damage was the mean of all corresponding

Table 3 | Predicted and observed response of stroke patients to neurotransmitter-modulating drugs

Case	Clinical presentation	Drug used	Predominant lesion-associated circuit disruption	Predicted response	Observed response
1 ¹⁴²	Poststroke cognitive and behavioral deficits	Donepezil (AChEI)	Presynaptic	Improvement	Improvement
2 ¹⁴³	Poststroke parkinsonism	Cabergoline (DA)	Presynaptic	Improvement	Improvement
3 ¹⁴⁴	–	Piribedil (DA)	Postsynaptic	No response	Improvement
4 ¹⁴⁵	–	Pramipexole (DA)	Presynaptic	Improvement	Improvement
5 ¹⁴⁶	–	Pramipexole (DA)	Presynaptic	Improvement	Improvement
6 ¹⁴⁷	–	Bromocriptin (DA)	Postsynaptic	No response	No response
7 ¹⁴⁸	Poststroke pathological laughing and crying	Paroxetine (SSRI)	Postsynaptic	Improvement	Improvement
8 ¹⁴⁹	–	Fluoxetine (SSRI)	Presynaptic	No response	Improvement
9 ¹⁵⁰	–	Fluoxetine (SSRI)	Presynaptic	No response	Improvement
10 ¹⁵¹	–	Sertraline (SSRI)	Postsynaptic	Improvement	Improvement
11 ¹⁵²	–	Paroxetine (SSRI)	Postsynaptic	Improvement	Improvement
12 ¹⁵²	–	Paroxetine (SSRI)	Postsynaptic	Improvement	Improvement
13 ¹⁵³	–	Escitalopram (SSRI)	Presynaptic	No response	No response
14 ¹⁵³	–	Escitalopram (SSRI)	Presynaptic	No response	No response
15 ¹⁵³	–	Sertraline (SSRI)	Presynaptic	No response	No response
16 ¹⁵⁴	–	Sertraline (SSRI)	Postsynaptic	Improvement	Improvement
17 ¹⁵⁵	Poststroke apathy	Ropinirole (DA)	Presynaptic	Improvement	Improvement
18 ^{156*}	–	Bupropion (DNRI)	Postsynaptic	Improvement	Improvement
19 ^{156*}	–	Donepezil (AChEI)	Presynaptic	Improvement	Improvement
20 ¹⁵⁷	–	Ropinirole (DA)	Postsynaptic	No response	Improvement
21 ^{158#}	–	Donepezil (AChEI)	Postsynaptic	No response	No response
22 ^{158#}	–	MPH (DNRI)	Postsynaptic	Improvement	No response

* and # Represent cases that reported the response to two different drugs. AChEI acetylcholinesterase inhibitors, DA dopamine receptor agonists, DNRI dopamine and noradrenaline reuptake inhibitor, MPH methylphenidate, SSRI selective serotonin reuptake inhibitor.

receptors postsynaptic structural damage. The formula for the postsynaptic ratio was as follows:

$$\text{postsynaptic ratio} = \frac{\max \left(\frac{\sum_{i \in R} M^{\text{recep_loc}}_i}{\sum_{i \in T} M^{\text{recep_loc}}_i}, \frac{\sum_{i \in R} M^{\text{recep_tract}}_i}{\sum_{i \in T} M^{\text{recep_tract}}_i} \right)}{\max \left(\frac{\sum_{i \in R} M^{\text{trans_loc}}_i}{\sum_{i \in T} M^{\text{trans_loc}}_i}, \frac{\sum_{i \in R} M^{\text{trans_tract}}_i}{\sum_{i \in T} M^{\text{trans_tract}}_i} \right)}$$

where: i , voxel value; max, maximum; M , lesion mask voxels; $n(R)$, number of receptors belonging to a certain neurotransmitter system; R , group of receptors belonging to a certain neurotransmitter system; recep_loc, receptor location density map; recep_tract, receptor white matter projection map; T , all map voxels; trans_loc, transporter location density map; trans_tract, transporter white matter projection map.

The NeuroT-Map tool, coded in Python and Bash, was created to calculate brain lesions' pre and postsynaptic ratios. The code is freely available at <https://github.com/Pedro-N-Alves/NeuroT-Map> (DOI: 10.5281/zenodo.14712890)

Clustering neurotransmitter profiles of stroke lesions

Two sets of stroke lesions were used in this analysis. The first set (the training set) was composed of 1333 ischemic stroke lesions of patients admitted to the University College London Hospitals (UCLH) acute stroke service^{42,125}. The patients' ages ranged from 18 to 97 years, with a mean of 64. The proportion of participants of male sex was 0.56. All performed 1.5 or 3 Tesla MRI within two weeks of stroke onset. Their lesions were delimited in the diffusion-weighted imaging (DWI) sequence and normalized into the MNI space. The median lesion volume was 6.5 cm³ (interquartile range 1.6–19.9 cm³). The West

London and GTAC Research Ethics Committee approved this sample recruitment and the consentless use of fully anonymized data.

The second set (the validation set) was constituted of 143 stroke lesions (119 ischemic, 24 hemorrhagic) of patients admitted to the Washington University School of Medicine in St. Louis⁴³. The patients' ages ranged from 19 to 83 years, with a mean of 54. The proportion of participants of male sex was 0.45. All performed 3 Tesla MRI within 1 to 3 weeks after stroke onset. Their lesions were delimited based on FLAIR, T1, and T2 sequences and normalized into the MNI space. The median lesion volume was 21.8 cm³ (interquartile range 4.3–56.9 cm³). The Washington University in Saint Louis Institutional Review Board approved the study. All participants provided informed consent.

Both samples are broadly representative of the distribution of stroke lesions^{42,43}. In the source stroke population of the training set, DWI was routinely performed on most patients, constrained mainly by MRI contraindications and tolerability⁴². In the validation set, the study sample was contrasted with 1209 stroke patients from the source population. It did not differ in terms of stroke severity, lesion side, and frequency of aphasia, neglect, or motor impairment⁴³. As expected, the analysis of the spatial correlation between the two datasets' lesion density maps, using the neuromaps tool "compare_images"¹²⁶, showed that they were strongly correlated (Spearman's correlation = 0.72).

First, we analyzed the clustering tendency of these sets' pre and postsynaptic ratios using the Hopkins test, implemented in the pyclustertend toolkit (<https://pyclustertend.readthedocs.io/>). Values tending to 0 indicate a high clustering tendency, as opposed to higher values, namely of more than 0.3. Then, we used the elbow method, implemented in the Yellowbrick toolkit (<https://www.scikit-yb.org/>), to determine the optimal number of clusters. Finally, we computed the unsupervised k-means clustering algorithm of the scikit-learn toolkit (<https://scikit-learn.org/>)^{46,127}. The algorithm was fitted on the training

set and applied to assign cluster indexes to the validation set. The validation of the analysis in a sample from a different setting and population allows the external validity and generalizability assessment of our results¹²⁸.

The neurotransmitter ratio profile of each cluster was plotted on a natural logarithmic scale. The one-sample *t* test or the Wilcoxon test (according to data distribution) were used to test which neurotransmitter ratios were significantly greater than zero. A Bonferroni correction for multiple comparisons was applied (alpha level set at 0.0042 for statistical significance). Cohen's *d* statistic or its nonparametric equivalent were calculated to estimate the effect size of the statistically significant associations.

Behavioral and motor profiles of neurotransmitter clusters

The validation set included detailed behavioral and motor assessments in the acute phase (13 ± 4.9 days after stroke) and 3 months after stroke⁴³. We analyzed if the neurotransmitter clusters differed in these measures.

The evaluation tests, organized by domains, were: (a) visuospatial attention - star cancellation task (from the behavioral inattention test), Mesulam symbol cancellation test, and Posner task; (b) language - picture naming test, auditory word discrimination, auditory command performance, read sentence comprehension, nonword reading (from the Boston diagnostic aphasia examination), and semantic fluency (animals); (c) visuospatial memory - brief visuospatial memory test revised; (d) verbal memory - Hopkins verbal learning test revised; (e) motor functions - action research arm test, active range of motion test, and walking test; (f) depressive symptoms - geriatric depression scale. The test scores were scaled into zero to one interval - zero corresponding to the worst performance observed and one to the best. The mean or median scores, according to data distribution, were plotted.

Composite scores of each domain (visuospatial attention, language, visuospatial memory, verbal memory, motor functions, and depression) were calculated by averaging the scaled scores of the corresponding tests. To investigate if the composite scores differed between clusters, the Kruskal-Wallis test was calculated. The two-sided Dunn's test was applied to perform pairwise comparisons when statistically significant differences occurred. A Bonferroni correction for multiple comparisons was applied (alpha level set at 0.0018 for statistical significance).

We also performed a UMAP analysis. UMAP is a technique for reducing the dimensionality of high-dimensional datasets, preserving their essential structure when mapped to a lower-dimensional space⁴⁴. It has demonstrated a better predictive capacity of stroke clinical deficits from structural disconnectome data⁴⁵. We applied the algorithm available at <https://umap-learn.readthedocs.io>. The default values of 15 for the size of the local neighborhood and 0.1 for the effective minimum distance between embedded points were used. The scaled behavioral and motor data was used as input. The HDBSCAN algorithm (available at <https://hdbscan.readthedocs.io/>) was applied to cluster the UMAP representation, as recommended (<https://umap-learn.readthedocs.io>)⁴⁶. The Adjusted Rand Score assessed the matching between the neurochemical and UMAP-derived behavioral and motor clusters (<https://scikit-learn.org/>)¹²⁷. A sensitivity analysis was also performed, including only the patients with no missing data.

Anatomical patterns of neurochemical clusters

The Disconnectome maps tool, from the BCBtoolkit, was used to compute structural disconnection (<http://www.bcbi-lab.com>)⁴⁹. Each brain lesion mask was overlapped on a group of 178 normative 7 T tractograms from the Human Connectome Project dataset¹¹⁹. Deterministic tractography was processed as specified in ref. 120. A map representing the voxel-wise probability of disconnection for each lesion was obtained.

Each cluster's lesions and structural disconnectome maps were contrasted with the remaining using 'randomise'^{129,130}. Nonparametric two-sample unpaired comparisons were performed based on permutations ($n = 5000$). A threshold-free cluster enhancement was applied, and the obtained *p*-values were family-wise error-corrected for multiple comparisons.

Validation of synaptic ratio analysis

We used PubMed (<https://pubmed.ncbi.nlm.nih.gov/>) to systematically search for stroke cases reporting the clinical response to neurotransmitter-modulating drugs and with images of lesion topography available. The following searching formulas were applied using both "All fields" and "MeSH Terms" filters: (a) "stroke" AND "cognition" AND ("cholinesterase inhibitor" OR "donepezil" OR "galantamine" OR "rivastigmine"); (b) "stroke" AND "parkinsonian disorder" AND ("dopamine agonists" OR "bromocriptine" OR "pramipexole" OR "ropinirole" OR "rotigotine"); (c) "stroke" AND ("pathological laughing and crying" OR "pseudobulbar affect") AND ("selective serotonin reuptake inhibitor" OR "citalopram" OR "escitalopram" OR "fluoxetine" OR "paroxetine" OR "sertraline"); (d) "stroke" AND "apathy" AND ("cholinesterase inhibitor" OR "donepezil" OR "galantamine" OR "rivastigmine" OR "dopamine agonists" OR "bromocriptine" OR "pramipexole" OR "ropinirole" OR "rotigotine" OR "selective serotonin reuptake inhibitor" OR "citalopram" OR "escitalopram" OR "fluoxetine" OR "paroxetine" OR "sertraline"). The systemic search retrieved 148 results. An additional free search was performed based on the references found and recent reviews. Fourteen case reports and 3 case series were selected, comprising a total of 20 stroke cases. Lesion masks were manually delineated in the MNI152 2 mm brain template in the same slices and orientations reported in the manuscripts. This method of lesion mapping has been widely used in lesion network mapping, and also in structural connectivity studies¹³¹⁻¹³⁴.

The Fisher exact test was applied to investigate the association between the NeuroT-map tool-based predicted pharmacological response and the response observed clinically.

Drugs were ranked according to their corresponding synaptic ratio in each graph to establish improvement likelihood ranks. The ranks varied from 1 to 6, denoting the six possible drug classes: predominantly pre or postsynaptic action in acetylcholinergic, dopaminergic, and serotonergic circuits. The highest synaptic ratio received a rank of 1, and the lowest synaptic ratio received a rank of 6. Therefore, ranks closer to 1 represented a higher probability of improvement with the administered drug. The Mann-Whitney test was computed to compare the drug improvement likelihood ranks between patients who clinically improved and those who did not.

Reporting summary

Further information on research design is available in the Nature Portfolio Reporting Summary linked to this article.

Data availability

Normative neurotransmitter receptor and transporter location density maps are available at https://github.com/netneurolab/hansen_receptors. The projection maps for each receptor and transporter are available at <https://identifiers.org/neurovault.collection:15237> and <https://identifiers.org/neurovault.collection:17228>. The raw MRI diffusion dataset is available at <https://www.humanconnectome.org>. The processed tractographies are available at <https://osf.io/5zqwq/> and https://storage.googleapis.com/bcblabweb/open_data.html. Source data are provided in this paper.

Code availability

The code of the Functionnectome tool is available at <https://github.com/NotaCS/Functionnectome>. The code of the NeuroT-Map tool is

available at <https://github.com/Pedro-N-Alves/NeuroT-Map> (<https://doi.org/10.5281/zenodo.14712890>).

References

- Cook, J. S. Spark' vs. 'Soup': A Scoop for soup for Soup. *Physiology* **1**, 206–208 (1986).
- Valenstein, E. S. The discovery of chemical neurotransmitters. *Brain Cogn.* **49**, 73–95 (2002).
- Loewi, O. Über humorale übertragbarkeit der Herznervenwirkung. *Pflugers Arch. Eur. J. Physiol.* **189**, 239–242 (1921).
- Dale, H. H., Feldberg, W. & Vogt, M. Release of acetylcholine at voluntary motor nerve endings. *J. Physiol.* **86**, 353–380 (1936).
- Carlsson, A., Lindqvist, M. & Magnusson, T. 3,4-Dihydroxyphenylalanine and 5-Hydroxy- tryptophan as reserpine antagonists. *Nature* **180**, 1200 (1957).
- Kebabian, J. W., Petzold, G. L. & Greengard, P. Dopamine-sensitive adenylate cyclase in caudate nucleus of rat brain, and its similarity to the 'Dopamine Receptor'. *Proc. Natl. Acad. Sci. USA* **69**, 2145–2149 (1972).
- Kandel, E. R. & Schwartz, J. H. Molecular biology of learning: Modulation of transmitter release. *Science* (1979) **218**, 433–443 (1982).
- Ballinger, E. C., Ananth, M., Talmage, D. A. & Role, L. W. Basal forebrain cholinergic circuits and signaling in cognition and cognitive decline. *Neuron* **91**, 1199–1218 (2016).
- Missale, C., Nash, S. R., Robinson, S. W., Jaber, M. & Caron, M. G. Dopamine receptors: From structure to function. *Physiol. Rev.* **78**, 189–225 (1998).
- Mesulam, M.-M., Mash, D., Hersh, L., Bothwell, M. & Geula, C. Cholinergic innervation of the human striatum, globus pallidus, subthalamic nucleus, substantia nigra, and red nucleus. *J. Comp. Neurol.* **323**, 252–268 (1992).
- Charnay, Y. & Léger, L. Brain serotonergic circuitries. *Dialogues Clin. Neurosci.* **12**, 471–487 (2010).
- Holland, N., Robbins, T. W. & Rowe, J. B. The role of noradrenaline in cognition and cognitive disorders. *Brain* **144**, 2243–2256 (2021).
- Alves, P. N., Forkel, S. J., Corbetta, M. & Thiebaut de Schotten, M. The subcortical and neurochemical organization of the ventral and dorsal attention networks. *Commun. Biol.* **5**, 1343 (2022).
- Feigin, V. L. et al. Global, regional, and national burden of stroke and its risk factors, 1990–2019: A systematic analysis for the Global Burden of Disease Study 2019. *Lancet Neurol.* **20**, 1–26 (2021).
- Clarke, S. Identifying patterns of cognitive deficits: The path to better outcomes after stroke. *J. Neurol. Neurosurg. Psychiatry* **91**, 449–450 (2020).
- Weaver, N. A. et al. Strategic infarct locations for post-stroke cognitive impairment: a pooled analysis of individual patient data from 12 acute ischaemic stroke cohorts. *Lancet Neurol.* **20**, 448–459 (2021).
- Mayberg, H. S. et al. PET Imaging of cortical 2 serotonin receptors after stroke: Lateralized changes and relationship to depression. *Am. J. Psychiatry* **145**, 937–943 (1988).
- O'Sullivan, M. J., Oestreich, L. K. L., Wright, P. & Clarkson, A. N. Cholinergic and hippocampal systems facilitate cross-domain cognitive recovery after stroke. *Brain* **145**, 1698–1710 (2022).
- Geranmayeh, F. Cholinergic neurotransmitter system: A potential marker for post-stroke cognitive recovery. *Brain* **145**, 1576–1578 (2022).
- Legg, L. A. et al. Selective serotonin reuptake inhibitors (SSRIs) for stroke recovery. *Cochrane Database Syst. Rev.* **11**, CD009286 (2019).
- Dennis, M. et al. Effects of fluoxetine on functional outcomes after acute stroke (FOCUS): a pragmatic, double-blind, randomised, controlled trial. *Lancet* **393**, 265–274 (2019).
- Kalbounieh, H. M., Toubasi, A. A., Albustanji, F. H., Obaid, Y. Y. & Al-Harasis, L. M. Safety and efficacy of SSRIs in improving poststroke recovery: A systematic review and meta-analysis. *J. Am. Heart Assoc.* **11**, e025868 (2022).
- Zhang, L. S. et al. Prophylactic effects of duloxetine on post-stroke depression symptoms: An open single-blind trial. *Eur. Neurol.* **69**, 336–343 (2013).
- Cravello, L., Caltagirone, C. & Spalletta, G. The SNRI venlafaxine improves emotional unawareness in patients with post-stroke depression. *Hum. Psychopharmacol.* **24**, 331–336 (2009).
- Sato, S., Yamakawa, Y., Terashima, Y., Ohta, H. & Asada, T. Efficacy of milnacipran on cognitive dysfunction with post-stroke depression: Preliminary open-label study. *Psychiatry Clin. Neurosci.* **60**, 584–589 (2006).
- Luvizutto, G. J. et al. Pharmacological interventions for unilateral spatial neglect after stroke. *Cochrane Database Syst. Rev.* **2015**, CD010882 (2015).
- Berthier, M. L. et al. A randomized, placebo-controlled study of donepezil in poststroke aphasia. *Neurology* **67**, 1687–1689 (2006).
- Ford, G. et al. Safety and efficacy of co-careldopa as an add-on therapy to occupational and physical therapy in patients after stroke (DARS): a randomised, double-blind, placebo-controlled trial. *Lancet Neurol.* **18**, 530–538 (2019).
- Hansen, J. Y. et al. Mapping neurotransmitter systems to the structural and functional organization of the human neocortex. *Nat. Neurosci.* **25**, 1569–1581 (2022).
- Puledda, F. et al. Abnormal glutamatergic and serotonergic connectivity in visual snow syndrome and migraine with aura. *Ann. Neurol.* **94**, 873–884 (2023).
- Funck, T. et al. 3D reconstruction of ultra-high resolution neurotransmitter receptor atlases in human and non-human primate brains. Preprint at <https://doi.org/10.1101/2022.11.18.517039> (2022).
- Nozais, V., Forkel, S. J., Foulon, C., Petit, L. & Thiebaut De Schotten, M. Functionnectome as a framework to analyse the contribution of brain circuits to fMRI. *Commun. Biol.* **4**, 1035 (2021).
- Lanciego, J. L. & Wouterlood, F. G. Neuroanatomical tract-tracing techniques that did go viral. *Brain Struct. Funct.* **225**, 1193–1224 (2020).
- Hornung, J.-P. The human raphe nuclei and the serotonergic system. *J. Chem. Neuroanat.* **26**, 331–343 (2003).
- van der Kooy, D. & Kuypers, H. G. Fluorescent retrograde double labeling: Axonal branching in the ascending raphe and nigral projections. *Science* **204**, 873–875 (1979).
- Mesulam, M.-M., Mufson, E. J., Levey, A. I. & Wainer, B. H. Cholinergic innervation of cortex by the basal forebrain: Cytochemistry and cortical connections of the septal area, diagonal band nuclei, nucleus basalis (Substantia Innominata), and hypothalamus in the Rhesus Monkey. *J. Comp. Neurol.* **214**, 170–197 (1983).
- Zaborszky, L. et al. Stereotaxic probabilistic maps of the magnocellular cell groups in human basal forebrain. *Neuroimage* **42**, 1127–1141 (2008).
- German, D., Bruce, G. & Hersh, L. Immunohistochemical staining of cholinergic neurons in the human brain using a polyclonal antibody to human choline acetyltransferase. *Neurosci. Lett.* **61**, 1–5 (1985).
- Takahashi, H., Nakashima, S., Ohama, E., Takeda, S. & Ikuta, F. Distribution of serotonin-containing cell bodies in the brainstem of the human fetus determined with immunohistochemistry using antiserotonin serum. *Brain Dev.* **8**, 355–365 (1986).
- Hirsch, E., Graybiel, A. & Agid, Y. Melanized dopaminergic neurons are differentially susceptible to degeneration in Parkinson's disease. *Nature* **334**, 345–348 (1998).
- Keren, N. I. et al. Histologic validation of locus coeruleus MRI contrast in post-mortem tissue. *Neuroimage* **113**, 235–245 (2015).

42. Bonkhoff, A. K. et al. Reclassifying stroke lesion anatomy. *Cortex* **145**, 1–12 (2021).
43. Corbetta, M. et al. Common behavioral clusters and subcortical anatomy in stroke. *Neuron* **85**, 927–941 (2015).
44. McInnes, L., Healy, J. & Melville, J. UMAP: Uniform Manifold Approximation and Projection for Dimension Reduction. Preprint at <https://doi.org/10.48550/arXiv.1802.03426> (2018).
45. Talozzi, L. et al. Latent disconnectome prediction of long-term cognitive-behavioural symptoms in stroke. *Brain* **146**, 1963–1978 (2023).
46. Pealat, C., Bouleux, G. & Cheutet, V. Improved time-series clustering with UMAP dimension reduction method. In *Proceedings - International Conference on Pattern Recognition* 5658–5665 (2020).
47. Zhao, Y., Halai, A. D. & Lambon Ralph, M. A. Evaluating the granularity and statistical structure of lesions and behaviour in post-stroke aphasia. *Brain Commun.* **2**, fcaa062 (2020).
48. Thiebaut de Schotten, M. & Forkel, S. J. The emergent properties of the connected brain. *Science* **378**, 505–510 (2022).
49. Foulon, C. et al. Advanced lesion symptom mapping analyses and implementation as BCBtoolkit. *Gigascience* **7**, 1–17 (2018).
50. Korczyn, A. D. Vascular parkinsonism-characteristics, pathogenesis and treatment. *Nat. Rev. Neurol.* **11**, 319–326 (2015).
51. Kim, J. O., Lee, S. J. & Pyo, J. S. Effect of acetylcholinesterase inhibitors on post-stroke cognitive impairment and vascular dementia: A meta-analysis. *PLoS ONE* **15**, <https://doi.org/10.1371/journal.pone.0227820> (2020).
52. Wortzel, H. S., Oster, T. J., Anderson, C. A. & Arciniegas, D. B. Pathological laughing and crying epidemiology, pathophysiology and treatment. *CNS Drugs* **22**, 531–545 (2008).
53. Tay, J., Morris, R. G. & Markus, H. S. Apathy after stroke: Diagnosis, mechanisms, consequences, and treatment. *Int. J. Stroke* **16**, 510–518 (2021).
54. Blaker, S. N., Armstrong, D. M. & Gage, F. H. Cholinergic neurons within the rat hippocampus: Response to Fimbria-Fornix Transection. *J. Comp. Neurol.* **272**, 127–138 (1988).
55. Gage, S. L., Keim, S. R., Simon, J. R. & Low, W. C. Cholinergic innervation of the retrosplenial cortex via the fornix pathway as determined by high affinity choline uptake, choline acetyltransferase activity, and muscarinic receptor binding in the rat. *Neurochem. Res.* **19**, 1379–1386 (1994).
56. Heschem, S. et al. Fornix deep brain stimulation enhances acetylcholine levels in the hippocampus. *Brain Struct. Funct.* **221**, 4281–4286 (2016).
57. Deeb, W. et al. Fornix-region deep brain stimulation-induced memory flashbacks in Alzheimer’s Disease. *N. Engl. J. Med.* **381**, 783–785 (2019).
58. Mamaligas, A. A., Barcomb, K. & Ford, C. P. Cholinergic transmission at muscarinic synapses in the striatum is driven equally by cortical and thalamic inputs. *Cell Rep.* **28**, 1003–1014 (2019).
59. Schwartz, M. L. & Mrzljak, L. Cholinergic innervation of the mediodorsal thalamic nucleus in the monkey: Ultrastructural evidence supportive of functional diversity. *J. Comp. Neurol.* **327**, 48–62 (1993).
60. Huerta-Ocampo, I., Hacıoglu-Bay, H., Dautan, D. & Mena-Segovia, J. Distribution of midbrain cholinergic axons in the thalamus. *eNeuro* **7**, 454 (2020).
61. Heckers, S., Geula, C. & Mesulam, M.-M. Cholinergic innervation of the human thalamus: Dual origin and differential nuclear distribution. *J. Comp. Neurol.* **325**, 68–82 (1992).
62. Green, S. M., Nathani, S., Zimmerman, J., Fireman, D. & Urs, N. M. Retrograde labeling illuminates distinct topographical organization of d1 and d2 receptor-positive pyramidal neurons in the prefrontal cortex of mice. *eNeuro* **7**, 194 (2020).
63. McCutcheon, R. A., Abi-Dargham, A. & Howes, O. D. Schizophrenia, dopamine and the striatum: From biology to symptoms. *Trends Neurosci.* **42**, 205–220 (2019).
64. Bromberg-Martin, E. S., Matsumoto, M. & Hikosaka, O. Dopamine in motivational control: Rewarding, aversive, and alerting. *Neuron* **68**, 815–834 (2010).
65. Pérez-Santos, I., Palomero-Gallagher, N., Zilles, K. & Cavada, C. Distribution of the noradrenaline innervation and adrenoceptors in the macaque monkey thalamus. *Cerebral Cortex* **31**, 4115–4139 (2021).
66. Carandini, T. et al. Disruption of brainstem monoaminergic fibre tracts in multiple sclerosis as a putative mechanism for cognitive fatigue: a fixel-based analysis. *Neuroimage Clin.* **30**, 102587 (2021).
67. Ventura, R., Cabib, S., Alcaro, A., Orsini, C. & Puglisi-Allegra, S. Norepinephrine in the prefrontal cortex is critical for amphetamine-induced reward and mesoaccumbens dopamine release. *J. Neurosci.* **23**, 1879–1885 (2003).
68. Arnsten, A. F. T., Wang, M. J. & Paspalas, C. D. Neuromodulation of thought: Flexibilities and vulnerabilities in prefrontal cortical network synapses. *Neuron* **76**, 223–239 (2012).
69. Hong, E. et al. Cholinergic left-right asymmetry in the habenulo-interpeduncular pathway. *Proc. Natl. Acad. Sci. USA* **110**, 21171–21176 (2013).
70. Pediconi, M. F., Roccamo De Fernfindez, A. M. & Barrantes, F. J. Asymmetric distribution and down-regulation of the muscarinic acetylcholine receptor in rat cerebral cortex. *Neurochem. Res.* **18**, 565–572 (1993).
71. Rodriguez, M., Martin, L. & Santana, C. Ontogenic development of brain asymmetry in dopaminergic neurons. *Brain Res. Bull.* **33**, 16–71 (1994).
72. Kranz, G. S. et al. Cerebral serotonin transporter asymmetry in females, males and male-to-female transsexuals measured by PET in vivo. *Brain Struct. Funct.* **219**, 171–183 (2014).
73. Tomer, R. et al. Dopamine asymmetries predict orienting bias in healthy individuals. *Cerebral Cortex* **23**, 2899–2904 (2013).
74. Michel, P. P., Toulorge, D., Guerreiro, S. & Hirsch, E. C. Specific needs of dopamine neurons for stimulation in order to survive: Implication for Parkinson disease. *FASEB J.* **27**, 3414–3423 (2013).
75. Toulorge, D. et al. Neuroprotection of midbrain dopamine neurons by nicotine is gated by cytoplasmic Ca²⁺. *FASEB J.* **25**, 2563–2573 (2011).
76. Benarroch, E. E. Pedunculopontine nucleus: Functional organization and clinical implications. *Neurology* **80**, 1148–1155 (2013).
77. Karachi, C. et al. Cholinergic mesencephalic neurons are involved in gait and postural disorders in Parkinson disease. *J. Clin. Invest.* **120**, 2745–2754 (2010).
78. Blier, P. & El-Mansari, M. Serotonin and beyond: Therapeutics for major depression. *Philos. Trans. R Soc. Lond. B Biol. Sci.* **368**, 20120536 (2013).
79. Done, C. J. & Sharp, T. Biochemical evidence for the regulation of central noradrenergic activity by 5-HT_{1A} and 5-HT₂ receptors: Microdialysis studies in the awake and anaesthetized rat. *Neuropharmacology* **33**, 411–421 (1994).
80. Zahrai, A., Vahid-Ansari, F., Daigle, M. & Albert, P. R. Fluoxetine-induced recovery of serotonin and norepinephrine projections in a mouse model of post-stroke depression. *Transl. Psychiatry* **10**, 334 (2020).
81. Hansen, J. Y. et al. Integrating brainstem and cortical functional architectures. *Nat. Neurosci.* **27**, 2500–2511 (2024).
82. Premi, E. et al. Unravelling neurotransmitters impairment in primary progressive aphasia. *Hum. Brain Mapp.* **44**, 2245–2253 (2023).
83. Hasselmo, M. E. The role of acetylcholine in learning and memory. *Curr. Opin. Neurobiol.* **16**, 710–715 (2006).

84. Coray, R. & Quednow, B. B. The role of serotonin in declarative memory: A systematic review of animal and human research. *Neurosci. Biobehav. Rev.* **139**, 104729 (2022).
85. Hauser, T. U., Eldar, E., Purg, N., Moutoussis, M. & Dolan, R. J. Distinct roles of dopamine and noradrenaline in incidental memory. *J. Neurosci.* **39**, 7715–7721 (2019).
86. Atucha, E. et al. Noradrenergic activation of the basolateral amygdala maintains hippocampus-dependent accuracy of remote memory. *Proc. Natl. Acad. Sci. USA* **114**, 9176–9181 (2017).
87. Nutt, D. J. Relationship of neurotransmitters to the symptoms of major depressive disorder. *J. Clin. Psychiatry* **69**, 4–7 (2008).
88. Caplan, L. R. & van Gijn, J. *Stroke Syndromes*. (Cambridge University Press, New York, 2012).
89. Ng, Y. S., Stein, J., Ning, M. M. & Black-Schaffer, R. M. Comparison of clinical characteristics and functional outcomes of ischemic stroke in different vascular territories. *Stroke* **38**, 2309–2314 (2007).
90. Bogousslavsky, J., Van Melle, G. & Regli, F. Original contributions the lausanne stroke registry: Analysis of 1000 consecutive patients with first stroke. *Stroke* **19**, 1083–1092 (1988).
91. Singh, N. et al. Prevalence and predictors of multivessel occlusions at baseline imaging in ESCAPE-NA1 trial. *Stroke* **54**, E233–E234 (2023).
92. Yen, C. P. et al. Simultaneous multiple hypertensive intracerebral haemorrhages. *Acta Neurochir.* **147**, 393–399 (2005).
93. Griffis, J. C., Metcalf, N. V., Corbetta, M. & Shulman, G. L. Structural disconnections explain brain network dysfunction after stroke. *Cell Rep.* **28**, 2527–2540 (2019).
94. Hillmer, A. T. et al. Imaging of cerebral $\alpha 4\beta 2^*$ nicotinic acetylcholine receptors with (–)-[18F]Flubatine PET: Implementation of bolus plus constant infusion and sensitivity to acetylcholine in human brain. *Neuroimage* **141**, 71–80 (2016).
95. Naganawa, M. et al. First-in-human assessment of 11c-lsn3172176, an m1 muscarinic acetylcholine receptor pet radiotracer. *J. Nucl. Med.* **62**, 553–560 (2021).
96. Aghourian, M. et al. Quantification of brain cholinergic denervation in Alzheimer's disease using PET imaging with [18F]-FEOBV. *Mol. Psychiatry* **22**, 1531–1538 (2017).
97. Bedard, M. A. et al. Brain cholinergic alterations in idiopathic REM sleep behaviour disorder: a PET imaging study with 18 F-FEOBV. *Sleep Med.* **58**, 35–41 (2019).
98. Kaller, S. et al. Test–retest measurements of dopamine D1-type receptors using simultaneous PET/MRI imaging. *Eur. J. Nucl. Med. Mol. Imaging* **44**, 1025–1032 (2017).
99. Alakurtti, K. et al. Long-term test-retest reliability of striatal and extrastriatal dopamine D2/3 receptor binding: Study with [11C]raclopride and high-resolution PET. *J. Cereb. Blood Flow Metab.* **35**, 1199–1205 (2015).
100. Smith, C. T. et al. Partial-volume correction increases estimated dopamine D2-like receptor binding potential and reduces adult age differences. *J. Cereb. Blood Flow Metab.* **39**, 822–833 (2019).
101. Jaworska, N. et al. Extra-striatal D2/3 receptor availability in youth at risk for addiction. *Neuropsychopharmacology* **45**, 1498–1505 (2020).
102. Sandiego, C. M. et al. Reference region modeling approaches for amphetamine challenge studies with [11C]FLB 457 and PET. *J. Cereb. Blood Flow Metab.* **35**, 623–629 (2015).
103. Dukart, J. et al. Cerebral blood flow predicts differential neurotransmitter activity. *Sci Rep* **8**, 1–11 (2018).
104. Sasaki, T. et al. Quantification of dopamine transporter in human brain using PET with 18F-FE-PE2I. *J. Nuclear Med.* **53**, 1065–1073 (2012).
105. Hesse, S. et al. Central noradrenaline transporter availability in highly obese, non-depressed individuals. *Eur. J. Nucl. Med. Mol. Imaging* **44**, 1056–1064 (2017).
106. Beliveau, V. et al. A high-resolution in vivo atlas of the human brain's serotonin system. *J. Neurosci.* **37**, 120–128 (2017).
107. Savli, M. et al. Normative database of the serotonergic system in healthy subjects using multi-tracer PET. *Neuroimage* **63**, 447–459 (2012).
108. Gallezot, J. D. et al. Kinetic modeling of the serotonin 5-HT 1B receptor radioligand 11 CP943 in humans. *J. Cereb. Blood Flow Metab.* **30**, 196–210 (2010).
109. Talbot, P. S. et al. Extended characterisation of the serotonin 2A (5-HT 2A) receptor-selective PET radiotracer 11C-MDL100907 in humans: Quantitative analysis, test-retest reproducibility, and vulnerability to endogenous 5-HT tone. *Neuroimage* **59**, 271–285 (2012).
110. Radhakrishnan, R. et al. Age-related change in 5-HT 6 receptor availability in healthy male volunteers measured with 11 C-GSK215083 PET. *J. Nucl. Med.* **59**, 1445–1450 (2018).
111. Nørgaard, M. et al. A high-resolution in vivo atlas of the human brain's benzodiazepine binding site of GABAA receptors. *Neuroimage* **232**, <https://doi.org/10.1016/j.neuroimage.2021.117878> (2021).
112. DuBois, J. M. et al. Characterization of age/sex and the regional distribution of mGluR5 availability in the healthy human brain measured by high-resolution [11C]ABP688 PET. *Eur. J. Nucl. Med. Mol. Imaging* **43**, 152–162 (2016).
113. Smart, K. et al. Sex differences in [11C]ABP688 binding: a positron emission tomography study of mGlu5 receptors. *Eur. J. Nucl. Med. Mol. Imaging* **46**, 1179–1183 (2019).
114. Kantonen, T. et al. Interindividual variability and lateralization of μ -opioid receptors in the human brain: Individual differences in the μ -opioid receptor system. *Neuroimage* **217**, 116922 (2020).
115. Turtunen, O. et al. Adult attachment system links with brain Mu opioid receptor availability in vivo. *Biol. Psychiatry Cogn. Neurosci. Neuroimaging* **6**, 360–369 (2021).
116. Gallezot, J. D. et al. Determination of receptor occupancy in the presence of mass dose: [11 C]GSK189254 PET imaging of histamine H 3 receptor occupancy by PF-03654746. *J. Cereb. Blood Flow Metab.* **37**, 1095–1107 (2017).
117. Normandin, M. D. et al. Imaging the cannabinoid CB1 receptor in humans with [11C] OMAR: Assessment of kinetic analysis methods, test-retest reproducibility, and gender differences. *J. Cereb. Blood Flow Metab.* **35**, 1313–1322 (2015).
118. Laurikainen, H. et al. Sex difference in brain CB1 receptor availability in man. *Neuroimage* **184**, 834–842 (2019).
119. Vu, A. T. et al. High resolution whole brain diffusion imaging at 7T for the Human Connectome Project. *Neuroimage* **122**, 318–331 (2015).
120. Thiebaut de Schotten, M., Foulon, C. & Nachev, P. Brain disconnections link structural connectivity with function and behaviour. *Nat. Commun.* **11**, 5094 (2020).
121. Tournier, J. D. et al. MRtrix3: A fast, flexible and open software framework for medical image processing and visualisation. *Neuroimage* **202**, 116137 (2019).
122. Jbabdi, S. & Johansen-Berg, H. Tractography: Where do we go from here? *Brain Connect* **1**, 169–183 (2011).
123. Calabrese, E., Badea, A., Cofer, G., Qi, Y. & Johnson, G. A. A Diffusion MRI tractography connectome of the mouse brain and comparison with neuronal tracer data. *Cerebral Cortex* **25**, 4628–4637 (2015).
124. Sotiropoulos, S. N. & Zalesky, A. Building connectomes using diffusion MRI: why, how and but. *NMR Biomed.* **32**, e3752 (2019).
125. Xu, T., Jager, H. R., Husain, M., Rees, G. & Nachev, P. High-dimensional therapeutic inference in the focally damaged human brain. *Brain* **141**, 48–54 (2018).
126. Markello, R. D. et al. Neuromaps: Structural and functional interpretation of brain maps. *Nat. Methods* **19**, 1472–1479 (2022).

127. Pedregosa, F. et al. Scikit-learn: Machine learning in Python. *J. Mach. Learn. Res.* **12**, 2825–2830 (2011).
128. Jung, A., Braun, T., Armijo-Olivo, S., Challoumas, D. & Luedtke, K. Consensus on the definition and assessment of external validity of randomized controlled trials: A Delphi study. *Res. Synth. Methods* **15**, 288–302 (2024).
129. Winkler, A. M., Ridgway, G. R., Webster, M. A., Smith, S. M. & Nichols, T. E. Permutation inference for the general linear model. *Neuroimage* **92**, 381–397 (2014).
130. Jenkinson, M., Beckmann, C. F., Behrens, T. E. J., Woolrich, M. W. & Smith, S. M. Fsl. *Neuroimage* **62**, 782–790 (2012).
131. Fox, M. D. Mapping symptoms to brain networks with the human connectome. *N. Eng. J. Med.* **379**, 2237–2245 (2018).
132. Joutsa, J., Horn, A., Hsu, J. & Fox, M. D. Localizing parkinsonism based on focal brain lesions. *Brain* **141**, 2445–2456 (2018).
133. Klingbeil, J. et al. Pathological laughter and crying: Insights from lesion network-symptom-mapping. *Brain* **144**, 3264–3276 (2021).
134. Alves, P. N., Silva, D. P., Fonseca, A. C. & Martins, I. P. Mapping delusions of space onto a structural disconnectome that decouples familiarity and place networks. *Cortex* **146**, 250–260 (2021).
135. Bianciardi, M. et al. A probabilistic template of human mesopontine tegmental nuclei from in vivo 7 T MRI. *Neuroimage* **170**, 222–230 (2018).
136. Björklund, A. & Dunnett, S. B. Dopamine neuron systems in the brain: an update. *Trends Neurosci.* **30**, 194–202 (2007).
137. García-Gomar, M. G. et al. Disruption of brainstem structural connectivity in REM sleep behavior disorder using 7 tesla magnetic resonance imaging. *Mov. Disord.* **37**, 847–853 (2022).
138. Edlow, B. L. et al. Neuroanatomic connectivity of the human ascending arousal system critical to consciousness and its disorders. *J. Neuropathol. Exp. Neurol.* **71**, 531–546 (2012).
139. Weinshenker, D. & Schroeder, J. P. There and back again: A tale of norepinephrine and drug addiction. *Neuropsychopharmacology* **32**, 1433–1451 (2007).
140. Bianciardi, M. et al. Toward an in vivo neuroimaging template of human brainstem nuclei of the ascending arousal, autonomic, and motor systems. *Brain Connect* **5**, 597–607 (2015).
141. Singh, K., García-Gomar, M. G. & Bianciardi, M. Probabilistic atlas of the mesencephalic reticular formation, isthmus reticular formation, microcellular tegmental nucleus, ventral tegmental area nucleus complex, and caudal-rostral linear raphe nucleus complex in living humans from 7 tesla magnetic resonance imaging. *Brain Connect* **11**, 613–623 (2021).
142. Riveros, R., Chabriet, H., Flores, R., Alvarez, G. & Slachevsky, A. Effects of donepezil on behavioral manifestations of thalamic infarction: A single-case observation. *Front. Neurol.* <https://doi.org/10.3389/fneur.2011.00016> (2011).
143. Akyol, A., Akyildiz, U. O. & Tataroglu, C. Vascular Parkinsonism: A case of lacunar infarction localized to mesencephalic substantia nigra. *Parkinsonism Relat. Disord.* **12**, 459–461 (2006).
144. Defer, G.-L. et al. Rest tremor and extrapyramidal symptoms after midbrain haemorrhage: clinical and 18F-dopa PET evaluation. *J. Neurol. Neurosurg. Psychiatry* **57**, 987–989 (1994).
145. Orta Daniel, S. J. & Ulises, R. O. Stroke of the substance nigra and parkinsonism as first manifestation of systemic lupus erythematosus. *Parkinsonism Relat. Disord.* **14**, 367–369 (2008).
146. Peluso, S. et al. Efficacy of dopamine agonist treatment in delayed-onset parkinsonism due to midbrain hemorrhage. *Parkinsonism and Relat. Disord.* **21**, 156–158 (2015).
147. Peters, S., Eising, E. G., Przuntek, H. & Müller, T. Vascular Parkinsonism: A case report and review of the literature. *J. Clin. Neurosci.* **8**, 268–271 (2001).
148. Derex, L., Ostrowsky, K., Nighoghossian, N. & Trouillas, P. Severe pathological crying after left anterior choroidal artery infarct: Reversibility with paroxetine treatment. *Stroke* **28**, 1464–1466 (1997).
149. Gondim, A., Thomas, F. P. & Cruz-Flores, S. Pathological laughter and crying: A case series and proposal for a new classification. *Ann. Clin. Psychiatry* **28**, 11–21 (2016).
150. Morland, D., Wolff, V., Blondet, C., Marescaux, C. & Namer, I. J. Pathological laughing: Brain SPECT findings. *Clin. Nucl. Med.* **40**, 734–736 (2015).
151. Okun, M. S., Riestra, A. R. & Nadeau, S. E. Treatment of Ballism and Pseudobulbar Affect With Sertraline. *Arch. Neurol.* **58**, 1682–1684 (2001).
152. Shimoda, K. & Kimura, M. Two cases of emotional disorder after middle cerebral artery infarction showing distinct responses to antidepressant treatment. *Neuropsychiatr. Dis. Treat.* **10**, 965–970 (2014).
153. Shin, S. H., Kim, Y. W. & Kim, N. Y. Treatment of poststroke pathologic laughing with duloxetine: A case series. *Clin. Neuropharmacol.* **42**, 60–63 (2019).
154. Takeuchi, H. et al. Effective use of sertraline for pathological laughing after severe vasospasm due to aneurysmal subarachnoid hemorrhage: Case report. *Neurol. Med. Chir.* **54**, 231–235 (2014).
155. Adam, R. et al. Dopamine reverses reward insensitivity in apathy following globus pallidus lesions. *Cortex* **49**, 1292–1303 (2013).
156. Ioannidis, A. E. et al. Apathy, cognitive dysfunction and impaired social cognition in a patient with bilateral thalamic infarction. *Neurocase* **19**, 513–520 (2013).
157. Kohno, N. et al. Successful treatment of post-stroke apathy by the dopamine receptor agonist ropinirole. *J. Clin. Neurosci.* **17**, 804–806 (2010).
158. Siegel, J. S. et al. The circuitry of abulia: Insights from functional connectivity MRI. *Neuroimage Clin.* **6**, 320–326 (2014).

Acknowledgements

P.N.A. is supported by the grants ‘Prémio João Lobo Antunes 2018—SCML’, ‘Prémio Maria de Sousa 2024 – Ordem dos Médicos e Fundação Bial’ and ‘Bolsa de Investigação em Doenças Vasculares Cerebrais 2017 – SPAVC’; P.N. is supported by Wellcome and the UCLH NIHR Biomedical Research Center; M.T.d.S. is supported by HORIZON-INFRA-2022 SERV (Grant No. 101147319) ‘EBRAINS 2.0: A Research Infrastructure to Advance Neuroscience and Brain Health’, by the European Union’s Horizon 2020 research and innovation program under the European Research Council (ERC) Consolidator grant agreement No. 818521 (DISCONNECTOME), the University of Bordeaux’s IdEx ‘Investments for the Future’ program RRI ‘IMPACT’, and the IHU ‘Precision & Global Vascular Brain Health Institute – VBHI’ funded by the France 2030 initiative (ANR-23-IAHU-0001). We thank Hans-Otto Karnath, MD, PhD, and Stephen Jackson, PhD, for their discussion and constructive feedback on our work during its presentation at a scientific meeting.

Author contributions

P.N.A. contributed to the conception and design of the work, analysis and interpretation of the data, creation of the software, and drafted the manuscript; V.N. contributed to the analysis of the data and substantively revised the manuscript; J.Y.H. contributed to the acquisition of the data and substantively revised the manuscript; M.C. contributed to the acquisition of the data; P.N. contributed to the acquisition of the data and substantively revised the manuscript; I.P.M. contributed to the conception and design of the work and substantively revised the manuscript; M.T.S. contributed to the conception and design of the work, analysis and interpretation of the data, and substantively revised the manuscript.

Competing interests

The authors declare no competing interests.

Additional information

Supplementary information The online version contains supplementary material available at <https://doi.org/10.1038/s41467-025-57680-2>.

Correspondence and requests for materials should be addressed to Pedro Nascimento Alves.

Peer review information *Nature Communications* thanks Christoph Sperber and the other anonymous reviewer(s) for their contribution to the peer review of this work. A peer review file is available.

Reprints and permissions information is available at <http://www.nature.com/reprints>

Publisher's note Springer Nature remains neutral with regard to jurisdictional claims in published maps and institutional affiliations.

Open Access This article is licensed under a Creative Commons Attribution-NonCommercial-NoDerivatives 4.0 International License, which permits any non-commercial use, sharing, distribution and reproduction in any medium or format, as long as you give appropriate credit to the original author(s) and the source, provide a link to the Creative Commons licence, and indicate if you modified the licensed material. You do not have permission under this licence to share adapted material derived from this article or parts of it. The images or other third party material in this article are included in the article's Creative Commons licence, unless indicated otherwise in a credit line to the material. If material is not included in the article's Creative Commons licence and your intended use is not permitted by statutory regulation or exceeds the permitted use, you will need to obtain permission directly from the copyright holder. To view a copy of this licence, visit <http://creativecommons.org/licenses/by-nc-nd/4.0/>.

© The Author(s) 2025